

THESIS

FEASIBILITY ASSESSMENT OF MAGNETIC SENSORS FOR MEASUREMENT OF HALL
CURRENT INDUCED CHANGES TO THE STATIC MAGNETIC FIELD NEARBY A HALL
THRUSTER

Submitted By

Zoe Morozko

Department of Mechanical Engineering

In partial fulfillment of the requirements

For the Degree of Master of Science

Colorado State University

Fort Collins, Colorado

Spring 2013

Master's Committee:

Advisor: John Williams

Mitchell Stansloski

Christopher Thornton

ABSTRACT

FEASIBILITY ASSESSMENT OF MAGNETIC SENSORS FOR MEASUREMENT OF HALL CURRENT INDUCED CHANGES TO THE STATIC MAGNETIC FIELD NEARBY A HALL THRUSTER

A Hall thruster is an electric propulsion device that produces thrust electrostatically by accelerating propellant to velocities 5 to 10 times higher than is achievable using conventional chemical thrusters. This is accomplished through the application of static, crossed electric and magnetic fields that are concentrated in a region close to the exit plane of the thruster. During operation an azimuthal plasma-electron current develops in the region where the electric and magnetic fields are concentrated. This embedded plasma current is referred to as the Hall current. The thrust produced from accelerating the propellant is transferred to a satellite or spacecraft through interaction between the Hall current and the magnetic coils used to produce the static magnetic field within the thruster. The Hall current can be calculated and the thrust can be determined in real time by measuring the magnetic field produced by the Hall current using sensors located external to the thruster. This work investigates the feasibility of placing magnetic sensors in the regions close to the exit of the thruster to measure the external magnetic field and correlate it to the Hall current. A finite element magnetic solver was used to identify several locations outside of the thrust plume and near the pole piece where the magnetic field magnitude changes by several Gauss in a background field level of ~50 Gauss. Magnetic sensors based on the giant magnetoresistive effect were identified as acceptable with regard to sensitivity, and measurements made with these sensors in a simulated high background magnetic field environment demonstrated that changes of 0.5 Gauss could be easily measured. This work also

presents the development of a thrust stand that will be useful in future work to demonstrate the overall concept. Special focus was directed to the design of the data acquisition system and in-vacuum calibration system used to make measurements with the thrust stand.

ACKNOWLEDGEMENTS

I feel that now would be an appropriate time to speak of travel. This work owes a lot to travel. The concepts and research conducted and discussed in this thesis may eventually lend themselves to space transportation. And I myself found that I had great distances to traverse and progress to make both geographically and personally, in concluding my work here. Whole continents were crossed, twice, in the conclusion of this thesis, which can rarely be done alone. Therefore, some acknowledgements are due.

Firstly, I would like to express my gratitude to Dr. John Williams who brought me across country with a wonderful opportunity to conduct research on something I love at the CSU Electrical Propulsion and Plasma Engineering Laboratory. I am grateful for his instruction and guidance through this experience. Thank you to Daisy Williams for her assistance and for all her computer help, and to Xie Kan for his patience and dedication in helping me grasp these fascinating concepts. And of course thanks are due to the other members of CEPPE Lab, for all the help they provided during this process: Lauren Rand, Nick Riedel, Casey Farnell, Cody Farnell, and anyone else who I may have frequently called upon for insight and wisdom.

Secondly, I would like to thank my friends and family, who stood behind me in my decision to cross this country again, to conclude my work here. Specifically, I would like to thank Robin Ward, for giving me strength, my sister, Eva Morozko, for giving me support, my grandfather, Pasquale Lombardi, for giving me guidance, my father, Bruce Morozko, for giving me focus, and most of all, my mother, Deborah Lombardi, for giving me inspiration.

And finally I would like to say thank you to Jetson. Because of him, I really never traveled alone.

TABLE OF CONTENTS

Abstract.....	ii
Acknowledgements.....	iv
Table of Contents.....	v
List of Figures.....	vii
Introduction.....	1
Propulsion.....	1
Electric Propulsion and Hall Thrusters.....	3
Focus of Research.....	9
Discussion of Research Implications.....	14
Thrust Stand.....	17
Background on Thrust Stands.....	17
CSU Thrust Stand.....	19
Description.....	19
Data Conditioning and Acquisition System.....	21
Calibration of the Thrust Stand.....	23
Determining Sensitivity.....	27
Typical Thrust Measurement of CSU Hall Thruster.....	30
Simulating Hall Current.....	34
Introduction to FEMM.....	35
Hall Current Simulation.....	37
Objective 1 Investigation.....	38
Objective 2 Investigation.....	43
Sensor Positioning Based on FEMM Analysis.....	47
Magnetic sensors.....	50

Magneto-resistive Sensors.....	51
Experimental Design and Validation.....	55
Validation of FEMM Calculations Using Sensors.....	60
Conclusion and Suggestions for Future Work.....	66
Conclusion.....	66
Future Work.....	67
Inverse Magneto-static Problem and Thrust Sensor.....	67
Sensor Array Design and Protection.....	68
Bibliography.....	69

LIST OF FIGURES

Figure 1-1 Cross sectional schematic diagram of a Hall thruster.	7
Figure 1-2 Hypothetical path of an electron in a crossed electric and magnetic field in a Hall thruster.	9
Figure 1-3 Laboratory Hall thruster in operation on xenon.	10
Figure 1-4 Illustration of Gaussmeter probe mapping region.	12
Figure 1-5 Map of magnetic field within discharge chamber of laboratory thruster model. The region mapped is identified in Fig. 1-5 where more details of the thruster are shown.	13
Figure 1-6 Typical FEMM output of magnetic field magnitude within the thruster. The black box represents the region that was mapped on the laboratory thruster.	13
Figure 1-7 Laboratory Hall thruster with hollow cathode.	14
Figure 1-8 Expansion of Eq. (1-7)(Rubin et. al., 2006).	15
Figure 1-9 Conceptual placement for non-contact magnetic sensor array.	16
Figure 2-1 Photograph of thrust stand.	20
Figure 2-2 Cross sectional diagram of the LVDT designed and employed for thrust stand displacement measurement.	22
Figure 2-3 Force transfer system for in- vacuum thrust stand calibration. The arrows, which are superimposed over the thin string connecting the weights to the stand, represent force transfer in the calibration system.	24
Figure 2-4 Diagram of force transfer in calibration system.	25
Figure 2-5 Cycles of weight application for calibration.	26
Figure 2-6 One cycle of weights being added and then removed as part of the in-vacuum calibration process.	26
Figure 2-7 LVDT signal for each weight of the calibration process with error bars set to the standard deviation of the LVDT signals.	28
Figure 2-8 Calibration curve gathered from averaging the voltage change per weight added over several cycles.	29
Figure 2-9 LVDT data over a period when the thruster was turned ‘on’ and ‘off’.	31

Figure 2-10 Calibration curve with equation of best fit measured after the test in Fig. 2-9 was completed.....	31
Figure 3-1 FEMM Axisymmetric Model of SPT100 Thruster. The red box indicates the area where magnetic field data were collected. The blue box shows the area where simulated Hall currents were placed. The + and – signs depict the direction of applied coil current.....	37
Figure 3-2 Hall current cross section simulated with a 2.54 cm diameter symmetrical section located near the acceleration region of the thruster. In this figure, configuration “B” is shown. Configuration “A” is the same but with a 1.27 cm diameter section.....	39
Figure 3-3 Hall current cross section modeled using 6 small, 0.127 cm diameter "wires" of current spaced equally around a 2.54 cm circle that was located near the acceleration region of the thruster. In this figure, configuration “D” is shown. Configuration “C” is the same only with a 1.27 cm ring diameter	39
Figure 3-4 Contour plot of magnetic field change between “Configuration D” with Hall current at 75 A, and the same thruster with zero Hall current, otherwise known as the “off” condition. Contours are at an equal spacing of 3 Gauss.	42
Figure 3-5 Difference in magnetic field magnitude between “Configuration D” and “Configuration B” at 75 Amps Hall current. Contour lines represent equal spacing of 0.15 Gauss	43
Figure 3-6 The red lines indicate where magnetic field magnitude data were taken for each test. The horizontal line is located at Z=5.58 cm or 0.19 cm above exit plane. The vertical red line is taken at R=7.11 cm. It is noted that a position along R=7.11cm between 0 and 1 cm above the pole piece would be a good sensor location.....	45
Figure 3-7 plot of Magnetic field magnitude along the exit plane of the thruster for three cases of Hall current simulation.	45
Figure 3-8 Plot of the magnitude of magnetic field along the R= 7.11 cm line for all three simulations of Hall current distribution, compared to the thruster “off” simulation.	46
Figure 3-9 Axial magnetic field along the Z=5.58 cm contour (with applied Hall current). Arrows on the figure illustrate field component that is plotted.	48
Figure 3-10 Radial magnetic field along the R=7.112 cm contour (with applied Hall current). Arrows on the figure illustrate field component that is plotted.	48
Figure 3-11 Change in axial magnetic field along the z=5.58 cm contour (with 75 A total Hall current in the configuration with 50/50% current split).....	49
Figure 3-12 Change in radial magnetic field along at the r=7.112 cm contour (with 75 A total Hall current in the configuration with 50/50% current split).....	49
Figure 4-1 Corbino disk illustrating anisotropic magnetoresistance (AMR).....	51

Figure 4-2 Changing path of current in a magnetoresistive sensor, when magnetic field is applied. The new path is signified by the blue arrow, while the original path (with no applied magnetic field) is shown by the black outlined arrow. The B-field detection direction is the same as in the Corbino disk.....	52
Figure 4-3 Layers of material in GMR elements (Caruso et al., 1998).	53
Figure 4-4 A diagram of the inside of a GMR magnetic sensor. The red resistors are fixed, and the blue resistors are made from the nano layered GMR material. The green arrows designate the direction of the magnetic field to be measured.	54
Figure 4-5 Axis of sensitivity provided by NVE Corporation GMR sensors (NVE, 2012).	55
Figure 4-6 Experimental facility for sensor testing.	56
Figure 4-7 Direction of motion of sensor relative to wires A and B.	56
Figure 4-8 AA002-02 sensor voltage vs. position for various currents.	58
Figure 4-9 Plot of calculated magnetic field at varying sensor positions and current based on Equation 4-1.....	58
Figure 4-10 Calibration curve for the AA002-02 sensor at an input voltage of 8.6 V.	59
Figure 4-11 Placement of permanent magnet for creating the desired magnetic field for the sensor. Also visible is the framework used to support the foil Faraday cage.....	61
Figure 4-12 Magnetic sensor response to magnetic field induced by 11.5 current flow.	62
Figure 4-13 (A) Sensor voltage versus position for each current assignment. (B) Magnetic field versus position using the calibration curve generated in Fig. 4-12. Total current is 11.5 A for each condition.	64
Figure 4-14 FEMM simulation results for three points that are ~1 centimeter apart from the simulated Hall current. These data points were taken from Location (3) in Fig. 3-7.....	65

1. INTRODUCTION

The focus of this work is on judging the feasibility of using magnetic field sensors to measure the Hall current and calculate the thrust of Hall-effect electric propulsion engines. The following sections contain background information and a discussion of the focus of this research.

1.1 Propulsion

Rocket behavior can be achieved in many ways including air exhausting from a balloon causing it to zip through the air, a person on roller blades throwing bowling balls, or by the combined action of the propellant delivery, combustion, and acceleration sub-systems present in conventional chemical rockets. Thrust and exhaust velocity are measures of performance of a rocket engine. The thrust or force produced by an engine is typically measured on a thrust stand, and it is proportional to the product of the flow rate and exhaust velocity of the propellant. In a practical sense, the thrust level is important to determine if a given propulsion system can lift a spacecraft through the Earth's atmosphere and into orbit, but, once a spacecraft is in orbit, this practical limitation is removed and lower thrust levels can be utilized to perform a given mission.

The question of how much propellant mass is required to perform a given mission leads one to consider the importance of the propellant exhaust velocity. This is explained in an intuitive manner below, but readers are referred to Hill and Peterson, 1992, for a more formal and mathematical treatment. To begin, recall that Newton proposed each action has an equal and opposite reaction. In other words, if one pushes on an object, then it pushes back. The impulse imparted to an object is the force times the number of seconds that the force was applied. This concept can be applied to rockets where one can visualize the propellant mass as the “pusher”

and the spacecraft with its propulsion system as the “pushee.” The mass of propellant expelled in a given maneuver multiplied by its velocity relative to the spacecraft is equal to the impulse, which has units of kg m/s or N s. This impulse is applied to the spacecraft causing it to move away from the propellant, and hence, the velocity of the spacecraft is changed by the action of the propellant, allowing the spacecraft to be maneuvered to a desired location. If one used 1 kg of propellant that was expelled at a relative velocity of 4000 m/s, then one would produce an impulse of 4000 kg m/s (or 4000 N s). If a total of 40,000 N s is required for a given mission, then 10 kg of propellant expelled at 4000 m/s would be required. The same mission of 40,000 N s could be achieved in many ways. One method would be to expel 20 kg of propellant at 2000 m/s, but this would cause more propellant to be used. Another method would be to expel 1 kg of propellant at 40,000 m/s. This is much more desirable because much less propellant is required, and so one can conclude that, from a propellant usage standpoint, high exhaust velocities are much better than lower exhausts velocities.

One question often asked is how rockets can be made better. Propulsion systems that utilize a minimum of propellant to perform a given mission are better in the sense that less propellant mass needs to be launched with the spacecraft. Current launch costs are between \$20,000 and \$30,000 per kg, and so there is a significant monetary incentive to reduce the amount of propellant that is required by a spacecraft. And the question of how to make propulsion systems better turns to the question of how to accelerate propellant to higher velocities.

To review conventional chemical rockets consider the high performance Saturn 5 rockets used to launch the Apollo spacecraft to the moon. In a Saturn 5 rocket, fuel and oxidizer are combined together at high pressure, combustion is initiated, and the hot, high-pressure

combustion products are accelerated through a nozzle at 1000's of kg/s at an effective exhaust velocity of ~2,600 m/s. One can determine the thrust and exhaust velocity that is produced based on mass and energy conservation, nozzle geometry, and propellant and oxidizer properties. Limitations of materials used in pumps and combustion chambers prevent the use of pressures above tens of MPa, which, along with the nozzle throat area and combustion temperature, fix the flow rate of propellant (Hill and Peterson, 1992). Similar to maximum pressure operation, one can only operate combustion chambers so hot before they fail, and hence the maximum exhaust velocity produced by a conventional rocket is limited to about 4,500 m/s. Therefore conventional combustion rockets, while very good at blasting spacecraft off the Earth, are limited in their ability to utilize propellant efficiently.

From the discussion above it is understandable that a certain appeal exists for a propulsion device that would require very little propellant. Notably, missions to deep space requiring large changes in velocity are limited by the excessive amount of propellant mass a conventional rocket system would have to carry. A lighter spacecraft capable of achieving the same mission without using so much fuel would obviously be preferred.

1.2 Electric Propulsion and Hall Thrusters

Electric propulsion (EP), developed to flight status in the 1960's, has enjoyed employment in the satellite orbit correction and station keeping market since the 1970's due to its high exhaust velocity. EP devices accelerate propellant mass using methods other than combustion. Methods range from (1) electrically heating propellant to (2) electrostatically accelerating charged propellant particles to (3) the use of magneto-plasma-dynamic acceleration processes. Instead of accelerating a propellant through a nozzle after the propellant has been first pressurized and heated to high temperatures, electrostatic EP devices ionize a fuel and accelerate

it to velocities that are unobtainable with a conventional rocket. This results in a high specific impulse as defined in Eq. (1-1) and Eq. (1-2) (Hill and Peterson, 1992) where I is the total impulse, M_p is the mass of propellant, g_e is the acceleration due to gravity at the surface of the Earth, \mathcal{T} is the thrust, u_{eq} is the average exhaust velocity, and \dot{m} is the mass flow rate of propellant.

$$I_{sp} = \frac{I}{M_p g_e} = \frac{u_{eq}}{g_e} \quad (1-1)$$

$$u_{eq} = \frac{\mathcal{T}}{\dot{m}} \quad (1-2)$$

Current EP systems produce very small thrust (on the order of 10's to 100's of mN) due to limitations on the power that is available to spacecraft. Here lies the tradeoff between EP devices and conventional chemical rockets. While an EP device requires less propellant mass, has a smaller mass, and a larger specific impulse, the overall thrust is miniscule and some missions can take a long time to complete.¹

As mentioned above, electric propulsion devices fall into three categories including electrothermal, electrostatic, and electromagnetic (Goebel and Katz, 2008). Electrothermal thrusters, such as resistojets and arcjets, provide thrust by thermally heating propellant using electrical power. Electrostatic thrusters, such as an ion or Hall-effect thrusters use applied electric potentials to accelerate ions to high velocities. Electromagnetic thrusters such as magnetoplasmadynamic (MPD) thrusters use a self-generated electromagnetic field to accelerate

¹ In some instances, however, when this thrust is compounded over months and years in a near field-free environment such as deep space, an EP device can help a craft obtain speeds much larger than a conventional rocket and finish some missions faster.

ionized propellant. In each case comparatively higher values of specific impulse result as compared to chemical rockets. Hall thrusters are the focus of this thesis and they operate in the 1600 sec range of specific impulse.

The Hall-effect thruster or more simply the Hall thruster relies on an applied magnetic field to operate; it falls into the electrostatic category because an electric field created by an applied anode voltage is what actually accelerates the ions (Goebel and Katz, 2008). The Hall thruster was originally derived from work on magnetrons and cross-field plasma sources. A strong following in the Soviet Union occurred in the 1960-70's that resulted in more development and service than in the United States, which favored the ion thruster instead (Choueiri, 2001). Hall effect thrusters use crossed electric and magnetic fields to create a plasma and accelerate ions to high velocity to create thrust (Sommerville et al., 2011).

The Hall thruster considered in this thesis is cylindrical, and a cross section is shown in Fig. 1-1. At the heart of the thruster concept is crossed electric and magnetic fields. Both natural magnets and electric magnets (produced by flowing current through coils of wire) have been used. Electric magnets are used in the laboratory thruster at CSU for this research. The body of a Hall thruster is built using both ferrous and non-ferrous steel. Electric magnet coils are located at the center, and around the outside of the annular channel region where ions are produced and accelerated. The magnet coils are used to create a magnetic field that radially expands outward from the ferrous steel center pole piece towards the outer pole piece. Of course, the magnetic field has axial components as well, but the goal is to achieve a strong magnetic field in the radial direction near the downstream end of the thruster. The electric field is created near the concentrated radial magnetic field region by an electric potential that is applied between an anode in the bottom of the thruster, and a cathode, located after the exit plane. The anode

typically contains small apertures where propellant is provided for ionization by the electrons that are pulled from the cathode through the acceleration channel to the anode. Some propellant is also provided to the cathode where a plasma-bridge-neutralization path is formed from the cathode to the regions downstream of the acceleration zone.

The ionization of propellant and the motion of the ions in the thruster can cause erosion of the thruster. Two categories of Hall thruster have been developed and they include the Thruster with Anode Layer (TAL), which keeps the metal walls of the thruster short and bare, and the Stationary Plasma Thruster (SPT), which uses a ceramic to line the inner and outer walls of the acceleration channel (Wetch et al., 1995). Erosion of the channel surfaces is what most directly affects the life of a thruster (Mikellides et al., 2011), and each category of thruster has its benefits. The laboratory thruster used in this study was a knock off of an SPT 100. SPT thrusters are designated with a number value that corresponds to the outer diameter of the acceleration region in millimeters (Wetch et al., 1995).

The ceramic insulation channel used in the laboratory thruster was made from borosil. The first region of the insulation channel, which is closest to the anode, is called the ionization region, where the propellant exits the anode and becomes ionized. Further down the chamber is the acceleration region, where the ions are accelerated out of the thruster and produce the desired thrust.

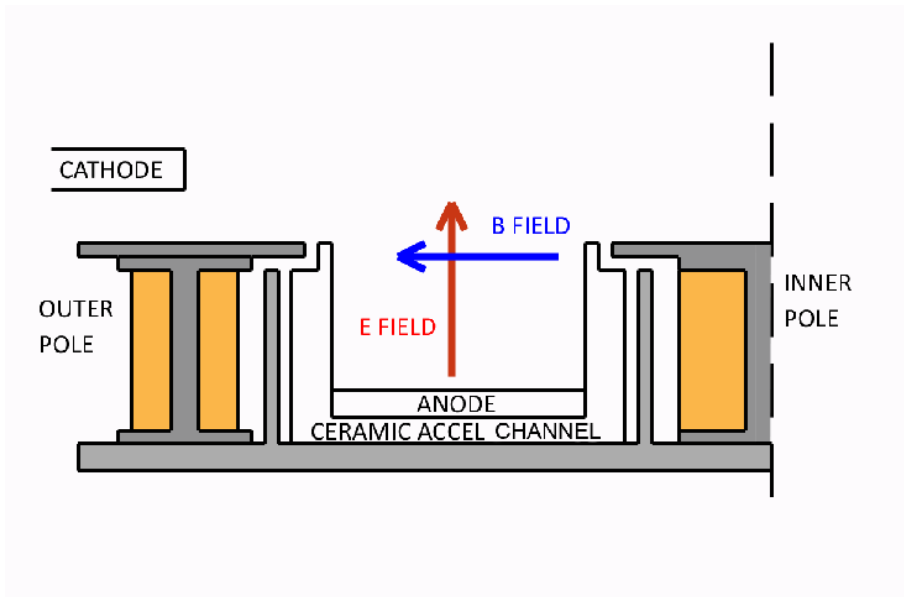


Figure 1-1 Cross sectional schematic diagram of a Hall thruster.

Edwin Hall, who discovered the Hall effect, found that when a charged particle is exposed to a magnetic field, it will alter the path of that particle. This can be explained in solid state physics using the concept of a Hall-based magnetic sensor. In this device, current is made to flow through a piece of material that is subjected to a strong magnetic field that is applied perpendicular to the current flow. The magnetic field causes charged particles flowing in the material to drift in the $E \times B$ direction (Kato et al., 2004). This change in path length can be measured and related to magnetic field strength. For the case of the Hall thruster, the Hall effect presents itself in the acceleration region of the thruster. The radial magnetic field and axial electric field cross at 90° to one another to produce an azimuthal drift velocity. This concept can be further described by examining the Lorentz force in Eq. (1-3).

$$F = q(E + \vec{V} \times \vec{B}) \quad (1-3)$$

Where F is the force on a charged particle, q is the charge of the particle, V is its velocity, B is the magnetic field, and E is the electric field. In Newton's second law, force is also defined by

$$F = m \frac{dv}{dt} \quad . \quad (1-4)$$

Under steady conditions the velocity (free drift) of the particle would be such that the force would be equal to zero, and then one could write

$$\vec{E} = -\vec{V}_{drift} \times \vec{B} \quad . \quad (1-5)$$

If both sides are crossed with B one could solve for the drift velocity

$$\vec{V}_{drift} = \frac{\vec{E} \times \vec{B}}{B^2} \quad . \quad (1-6)$$

Eq. (1-6) describes the drift velocity of an electron in the acceleration channel of a Hall thruster, and, although ions are also affected, their gyro radius is much larger than the electrons and they are not deflected much in the azimuthal direction (Goebel and Katz, 2008). The electrons that acquire the drift velocity move in a direction that is perpendicular to both the electric and magnetic fields. Superimposed upon this azimuthal drift velocity is a helical spiraling of the electrons around magnetic field lines and a slow collisional-induced diffusion of the electrons in the axial direction toward the anode. This complex motion is shown schematically in Fig. 1-2.

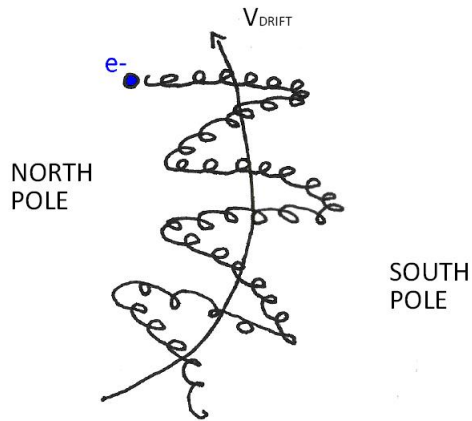


Figure 1-2 Hypothetical path of an electron in a crossed electric and magnetic field in a Hall thruster.

1.3 Focus of Research

When a Hall thruster is running, a glowing region of plasma appears within the ceramic channel as shown in Fig. 1-3. One can visualize the ring of electron current (the Hall current) that is circulating around the region just inside the channel exit plane and the ions that are being accelerated from the ionization region into the regions downstream of the thruster. There are two equivalent statements of how thrust is produced in a Hall thruster. The first is that a flow rate of ions is exiting the thruster at high velocity (after being accelerated by falling through a potential difference) and the thrust is simply the product of the ion flow rate and the average exhaust velocity. The second is that the ring of electron current (the Hall current) is producing a $J \times B$ force that is transferred to the electric magnets of the thruster. Technically one could measure the thrust in three different ways. First one could build a thrust stand and directly measure the thrust. Second one could very carefully measure the rate at which propellant is leaving the thruster and the average exhaust velocity using probes placed in the plume of the thruster. Third one could very carefully sense the Hall current and then integrate the product of the Hall current

density and the B-field over the volume of the acceleration region. This thesis uses the first technique and examines the requirements and feasibility of the third technique. The thrust stand was developed in this research activity to have very good sensitivity so that future work conducted on the third technique could be validated.

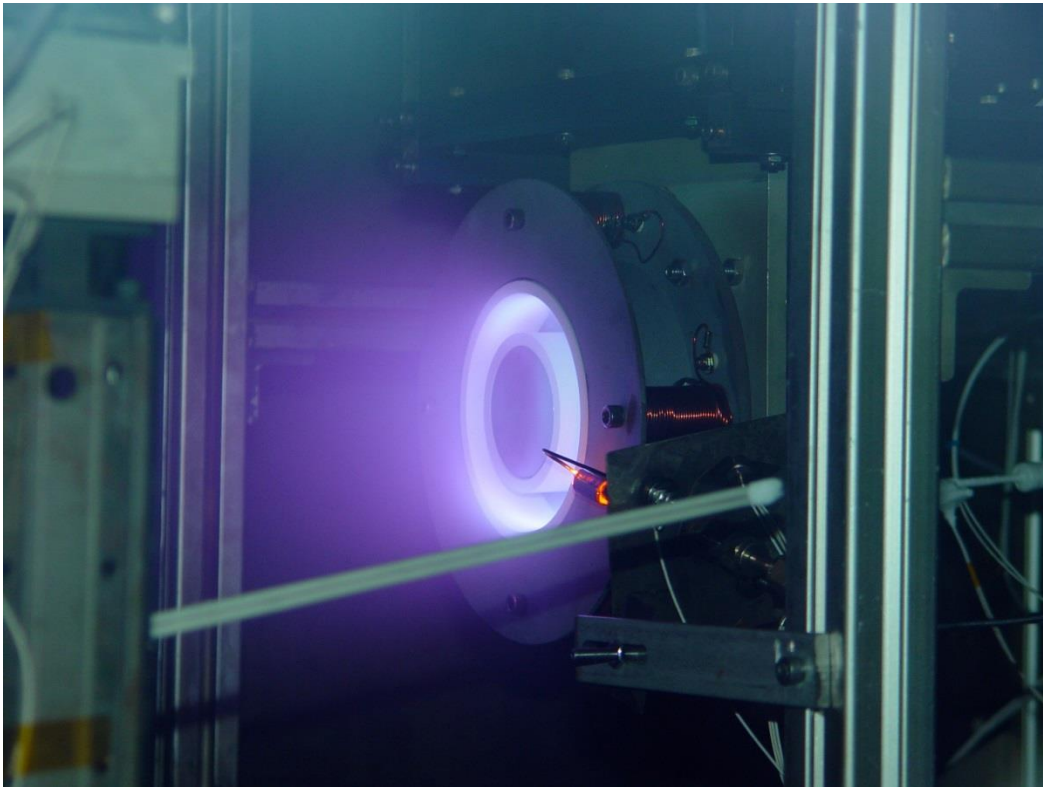


Figure 1-3 Laboratory Hall thruster in operation on xenon.

The Performance of a Hall thruster relies on the power sources available to operate it, the electric potential of the plasma produced, and the magnitude of the magnetic field and the Hall current. The contribution of the magnetic field to thruster performance can be in part described in Eq. (1-7),

$$AJ=B \quad , \quad (1-7)$$

where A is the matrix relating the Hall current distribution to the magnetic field distribution, J is a column vector representing the Hall current distribution, and B is the vector describing magnetic field distribution. The distribution of magnetic field throughout the channel can be calculated by a series of current elements created by the Hall current (Rubin, 2006). More discussion of this equation and its inverse is presented in Section 1.4.

By comparing the laboratory thruster model to other similar SPT100 type thrusters it was determined that a magnetic field of about 150 Gauss was necessary near the exit plane of the discharge chamber (Goebel and Katz, 2008). Achieving this field value is most directly associated with the thruster design. The materials chosen to construct the magnetic poles of the thruster, and the amount of current able to pass through the magnetic coil assembly before reaching saturation are key factors when trying to achieve the peak field. The magnetic components in the laboratory thruster used for the experiments covered in this thesis were made from 1018 steel. The center pole piece was machined from a solid piece of 1018 steel, and all magnetic coils were wound using 20 AWG copper magnet wire. Two tactics were employed to find the optimum geometry and coil current to produce the ideal magnetic field. Throughout this paper, use of a program called Finite Element Method Magnetics (FEMM) will be referenced. This open source computer program allows for two dimensional modeling of axisymmetric magnetic fields. The CSU thruster was modeled geometrically using a radial-axial geometry in FEMM. The modeling software uses current density applied to a cross sectional area to specify the coil current. Values for current density were adjusted until simulation results produced a peak field of 150 Gauss near the exit plane of the thruster. Based on the results from this program, the currents predicted for the CSU thruster were 1.5 A for the inner pole piece coil and 3.5 A in each

of the four outer pole piece coils. Orientation of the current direction dictated the direction of the magnetic field traveling from the inner north pole to the outer south pole.

The interior of the discharge chamber was mapped using a Gauss meter to check the accuracy of the FEMM simulation solutions for current assignment. The location mapped is illustrated in Fig. 1-4. A comparison of the simulated FEMM acceleration region and the mapped region is shown in Figs. 1-5 and 1-6. A photograph of the thruster is shown in Fig. 1-7 with labels of the various components so the reader can visualize the regions where the plots of Figs. 1-5 and 1-6 were created. It can be noted that a magnetic field value of about 150 Gauss is present near the central region of the acceleration zone in Fig. 1-5 and that a peak field of 220 Gauss lies near the center pole piece. Both of these values and the geometry of the magnetic field are similar to the results of the FEMM simulation shown in Fig. 1-6.

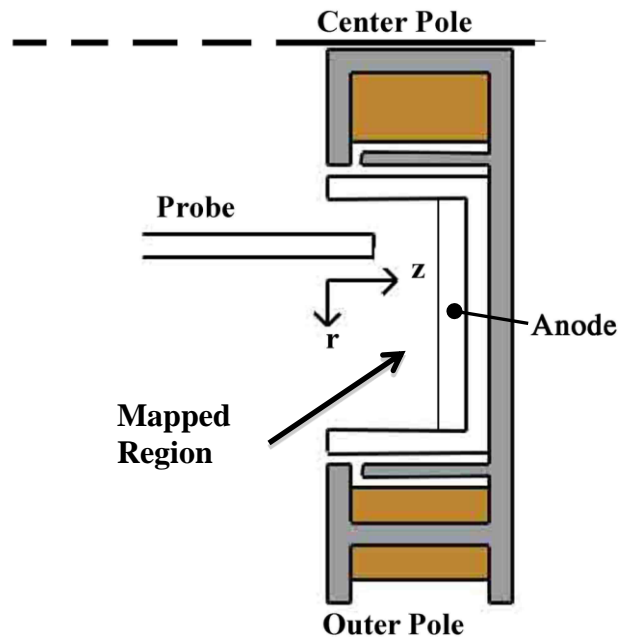


Figure 1-4 Illustration of Gaussmeter probe mapping region.

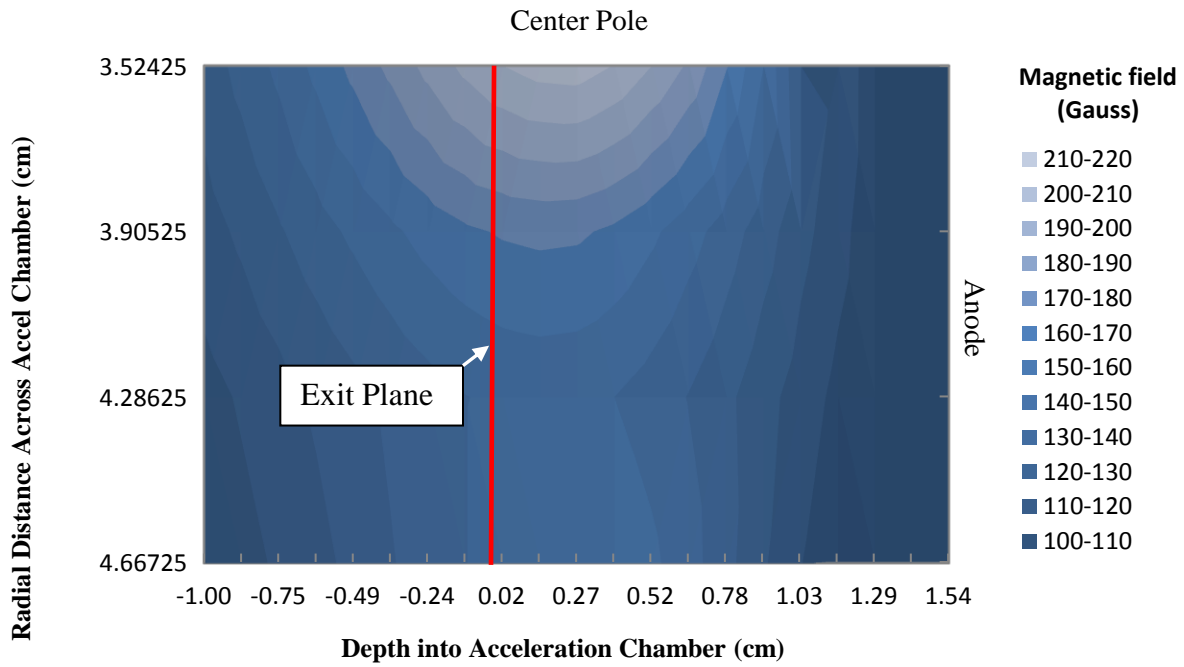


Figure 1-5 Map of magnetic field within discharge chamber of laboratory thruster model. The region mapped is identified in Fig. 1-5 where more details of the thruster are shown.

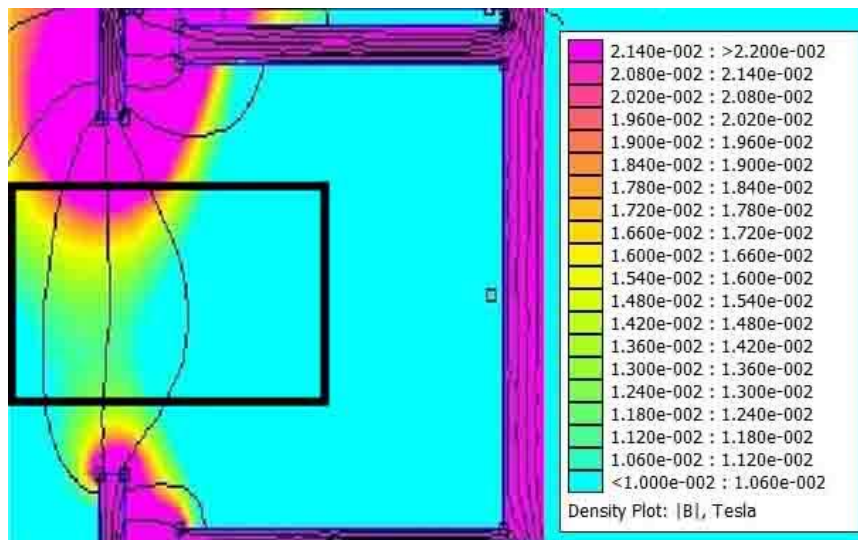


Figure 1-6 Typical FEMM output of magnetic field magnitude within the thruster. The black box represents the region that was mapped on the laboratory thruster.

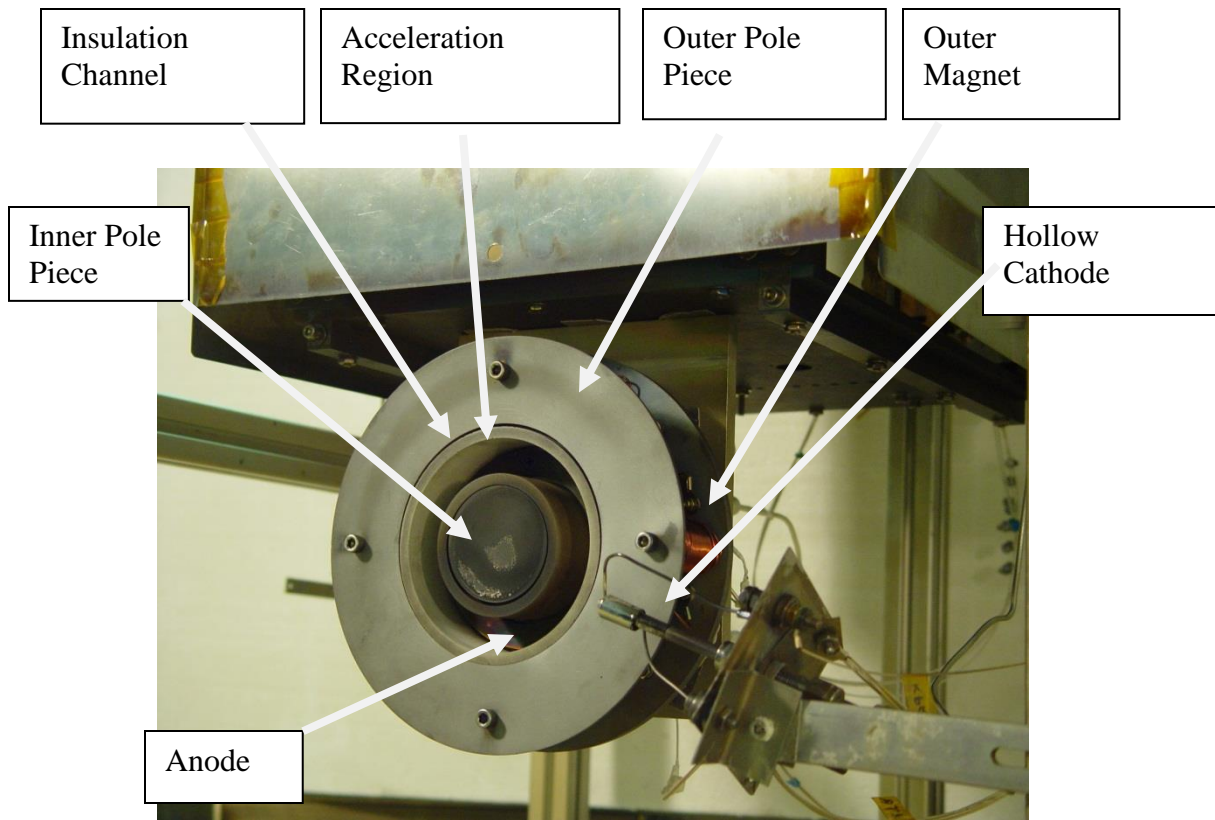


Figure 1-7 Laboratory Hall thruster with hollow cathode.

1.4 Discussion of Research Implications

It would be desirable to understand the performance of a Hall thruster both before flight and during its operation onboard a spacecraft. While a myriad of ways exist to test an EP device prior to operation in space, there are very few ways to monitor the operation of a thruster while it is in service other than to fire the thruster for a relatively long time and then measure the orbital changes that are induced in the trajectory of the spacecraft. This lack of real-time performance evaluation for a thruster can complicate the control of delicate maneuvers.

It is hypothesized that the use of remote magnetic sensors, placed in optimal positions and orientations, would enable collection of magnetic field data that could be used to determine

the Hall current and its structure. Figure 1-8 shows Eq. (1-7) in expanded form where one can see that data collected on the magnetic field can be used to solve inversely for the Hall current density. The thrust can then be found by integrating the cross product of the current density and the magnetic field over the volume of the acceleration region (Rubin, 2006).

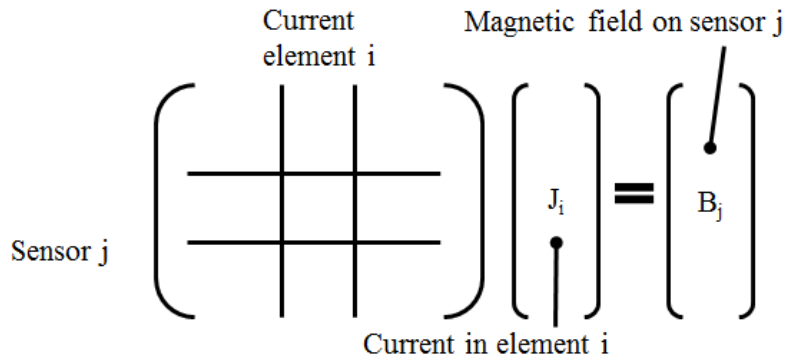


Figure 1-8 Expansion of Eq. (1-7) (Rubin et. al., 2006)

Solving the inverse problem shown in Fig. 1-8 requires reformatting Eq. (1-7) to create an error minimization problem, Eq. (1-8).

$$\text{Min} \|AJ - B_m\| \quad (1-8)$$

In Eq. (1-8) B_m is the vector of measured magnetic fields values provided by an array of magnetic sensor measurements. The elements of matrix A are the values of the magnetic field at different sensor locations generated by a current element. To calculate the magnetic field generated by a certain given element distribution, the A matrix is multiplied by the column vector J . The solution to such an inverse problem is an iterative process that requires advanced linear algebra techniques that are beyond the scope of this research.

Collecting these data would require either a series of sensors placed in an array, or a single sensor that is repositioned. This sensor development would need to withstand the

environment near the exit plane of the thruster, which includes bombardment from energetic ions, sputter coating from surrounding materials also bombarded by energetic ions, heat transfer from the thruster, and high magnetic fields near 50 Gauss at the surface of the thruster poles. A conceptual design for sensor placement with thruster hardware is shown in Fig. 1-9.

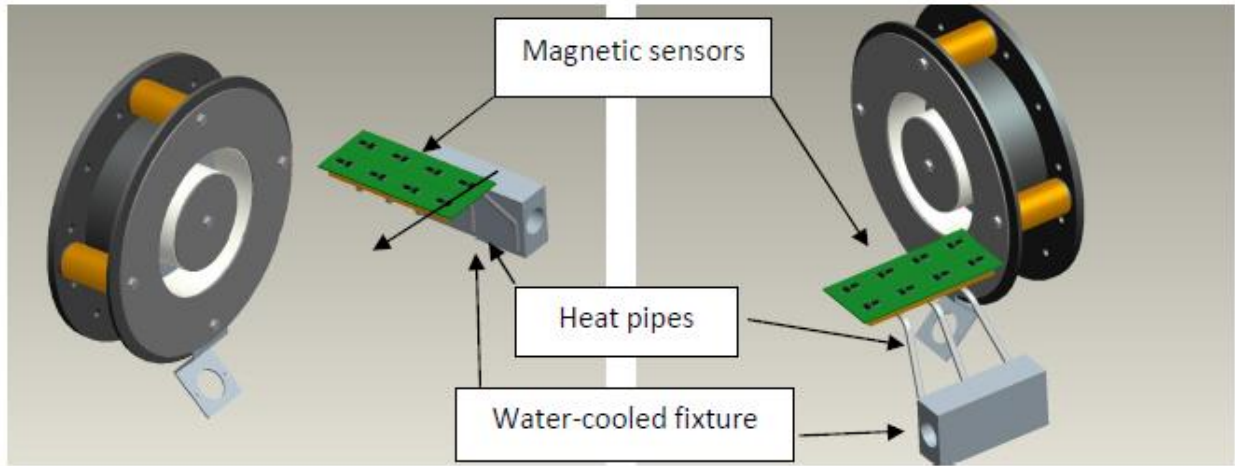


Figure 1-9 Conceptual placement for non-contact magnetic sensor array.

The process required to prove such a sensor array would be useful will first require the existence of a thrust stand capable of accurately measuring thrust. Next, it would be necessary to simulate the Hall current in a computer model like FEMM in such a way that the current could be reproduced in an actual thruster using a coil of wires. Comparisons between the FEMM calculations and experiments would verify that the sensors were working, and this exercise could be used to calibrate the overall sensor system. Making a sensor array part of the flight hardware package for a vehicle equipped with a Hall thruster would allow for real-time feedback of the thruster performance, and allow a satellite to be maneuvered more accurately. The remainder of this thesis presents the development and testing of a thrust stand, selection and testing of magnetic sensors, and modeling of the magnetic fields nearby Hall thrusters with simulated Hall current structures.

2. THRUST STAND

The focus of this chapter is on the description of a thrust stand developed at CSU that is based on a hanging double pendulum configuration whose motion is induced by the firing of a Hall thruster or by an in-vacuum calibration system and detected with a linear-variable-differential transformer (LVDT). The chapter is broken down into a section that contains background information on thrust stands used in electric propulsion research. Subsequent sections describe details of the CSU thrust stand construction, LVDT design and fabrication, data acquisition system set up, in-vacuum calibration, and determination of thrust stand sensitivity. Finally, a typical measurement of the thrust produced by the laboratory Hall thruster described in Chapter 1 is also presented.

2.1 Background on Thrust Stands

To validate the remote magnetic sensor concept in a laboratory setting, it is necessary to measure the thrust directly. Thrust stands are used for most thrust measurements of propulsion devices. In the case of the heavy lifting rockets such as the solid rocket boosters used on the space shuttle, a system of load cells is used on the structure supporting the boosters. The thrust produced by a Hall thruster, however, is too small for the load cell approach due to the thrust only being in the 0.1 N range. This means that thrust stands of very high sensitivity are required.

The low levels of thrust of electric propulsion devices lead to thrust stand designs that more closely resemble sensitive laboratory scales (Polzin et al., 2006). Most direct measurement designs fall into three categories: hanging pendulum, inverted pendulum, and torsional. The hanging pendulum design is the simplest and most stable design, usually used to test high thrust

to weight devices (Polzin et al., 2006). It relies on the basic idea that a perturbation will be stabilized by gravity resisting the displacement caused by thrust. Inverted pendulum designs display poorer performance when outside influences are present due to amplification of these influences (Moeller and Polzin, 2012). Although superior, hanging pendulum designs must overcome the mass of the pendulum and the thruster, and even though inherently stable operation is desirable, the magnitude of the hanging mass can reduce the sensitivity of the system. An inverted pendulum thrust stand has increased sensitivity over hanging pendulums as the mass of the system augments the displacement rather than the restoring force (Kodys et al., 2006). In most cases the inverted design consists of a pendulum arm anchored at the base with a material of known flexural bending strength. As the thruster at the top of the inverted pendulum fires, it disrupts the stability of the pendulum and the displacement is amplified as the pendulum moves. The flexural bending of the pivot point is relied on to dampen the motion and remove excess noise. To ensure linearity, however, most inverted thrust stands use a system of weights to return the thrust stand to the null vertical position, and the thrust is measured by recording the new position of the weight redistribution system.

It can be argued that torsional thrust stands provide the highest sensitivity since they can be made to be nearly independent of the thruster mass (Polzin et al., 2006). This design again places the thruster on the end of a pivot arm, which in this case swings through a plane parallel to the ground (perpendicular to the direction of the gravitational force). The measured displacement of the torsional arm is related to the thrust.

Finally, a fourth category of thrust measurement falls into the non-contact category, where methods using probes and sensors to measure the plasma density or magnetic field of a thruster are employed. Chapter 4 will further discuss this topic.

Ultimately, all methods of EP thrust measurement are being adapted and improved to be both sensitive and stable. A goal applicable to this research would be to produce a thrust stand that could reliably measure the thrust produced by a 1 kW laboratory Hall thruster to within ± 1 mN. Successful development of such a thrust stand would allow for accurate thruster data to be collected that could be compared to results from literature, and used to help validate a non-contact form of thrust measurement like the one described in Chapter 1. In the case of this thesis, a hanging pendulum thrust stand was already available.

2.2 CSU Thrust Stand

The thrust stand at CSU will be discussed below in three subsections. The first subsection describes the design of the stand itself, which includes electrical and gas connections as well as methods employed to shield it from effects that cause excessive noise. The second subsection contains a description of the LVDT and the data conditioning and acquisition system. Finally, a typical thrust measurement case is presented of a Hall thruster in which the calibration progress during the test was demonstrated.

2.3 Description

The thrust stand itself was built using 3.8cm x 3.8 cm aluminum bars to construct the framework. The stand fills a volume of about 46 cm x 46 cm x 76 cm. Graphite plates were machined for the top and bottom surfaces of the stand to hold the ends of thin, flexible, stainless steel ribbons that set the pivot points of a double pendulum. A mounting plate for the thruster was made from aluminum, and was attached to the bottom plate. The thrust stand is shown in Figure 2-1. The double pendulum design is useful to eliminate the need to know exactly where the center of the thrust vector is located because the relative motion of the bottom and top plate

at low thrust values is determined by the thrust and not the moment arm between the thrust vector and the pendulum pivot points.

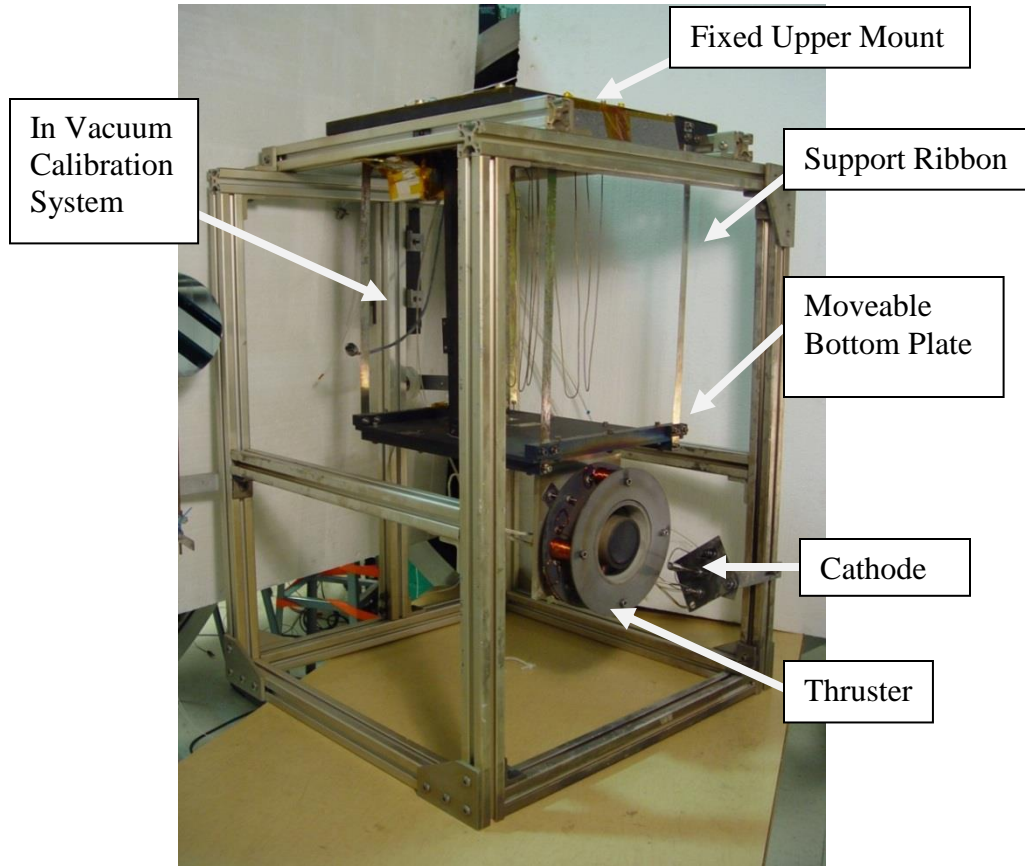


Figure 2-1 Photograph of thrust stand.

For the case of electrical and gas connections, all lines were worked through the top graphite plate to avoid interference with the swinging pendulum. The gas line was folded into a series of s-shaped sections to reduce its resistance to the motion of the pendulum. All electrical connections such as the cathode connection, the power lines leading to the thruster pole pieces, and power lines for controlling the calibration system were connected using a single, 22-pin connector. The anode power line was connected through a separate feed through to avoid the risk of arcing between the anode and the cathode within the 22-pin connector.

To prevent possible shorts between the thruster and the stand, and the cathode and the anode, precautions were made to isolate the thruster from all other surfaces. All screws used to attach the thruster to the stand were wrapped in Teflon tape, and surrounded by mica washers. Alumina ceramic tubes were used to insulate the anode gas feed line and the screws attaching the thruster to the stand. Finally, once the thruster was put in place, the entire upper portion of the thrust stand was surrounded in stainless steel, to form a Faraday cage around the linear-variable-differential transformer (LVDT), which was used to measure the displacement of the thrust stand.

2.4 Data Conditioning and Acquisition System

The popular method for measuring displacement of an EP thrust stand is with a LVDT, which consists of a ferromagnetic core that passes through a set of solenoid coils as shown schematically in Fig. 2-2. The outer secondary coils of the solenoid are wound in series. A sinusoidal oscillating current is passed through the center primary coil and as the core is displaced due to thruster action, it causes a voltage change to be registered in the secondary coils. Measuring this voltage change can be related to a known force value through calibration. An LVDT possesses a linear region in which the voltage change is directly related to the displacement. Outside this linear region, the LVDT becomes inaccurate; therefore it is important to select LVDT design parameters that allow for the necessary range of displacement.

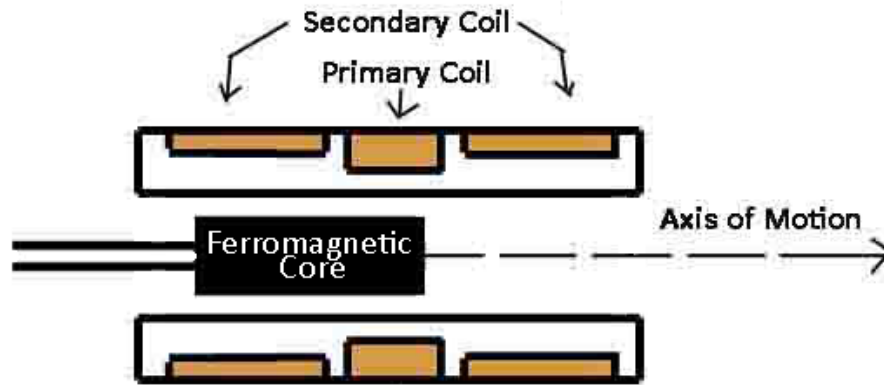


Figure 2-2 Cross sectional diagram of the CSU LVDT designed and employed for thrust stand displacement measurement.

The LVDT core was set to 2.54 cm long with a diameter of 0.647 cm. It was mounted on a rigid arm attached to the hanging pendulum. This arm placed the core up near the top plate of the stand. This placement allowed for less interference on the pendulum itself and reduced noise pick up from the environment. The outer windings were wound around a fiberglass-epoxy (G10) tube with an inner diameter of 1.18 cm and outer diameter of 1.97 cm. The coils were designed based on the work of Al Sharif, et al., 2011 where it was shown that LVDT sensitivity increased with secondary length, but decreased with primary length. Therefore it was determined that an LVDT design with a long secondary winding, measuring 1.92 cm in length, yet a shallow depth, with only an inner diameter of 1.73cm would be used. A short and deep primary coil, measuring 0.889 cm in length and 1.47 cm inner diameter provided the linear region of voltage measurement desired for the thrust range predicted of the laboratory thruster. This LVDT geometry was modeled using the Finite Element Method Magnetics program that was used to model the thruster, and adjusted after fabrication to find the ideal location of linearity. The LVDT coils were enclosed and shielded in a stainless steel box and wrapped in Kapton tape. Excitation of the primary coil and conditioning of the secondary signal was done with an SRS

lock-in amplifier using coaxial cable connections. The voltage change registered by the LVDT on the SRS amplifier was recorded using an Agilent 34970A data logger and a LabView program.

2.5 Calibration of the Thrust Stand

Many factors can affect the thrust stand causing it to drift and change sensitivity. For example, one of the stainless ribbons might heat up differently than the other ribbons and cause movement of the stand and the LVDT core. Reliable operation of the thrust stand, however, requires that the LVDT system register a change in voltage to a known applied force while drift and sensitivity changes are occurring. To achieve this result, an in-vacuum system of masses were used to calibrate the thrust stand before and after a thruster is operated.

There have been many methods employed to accurately calibrate a thrust stand to provide low error thrust measurements. Methods include use of nulling forces, which act to return a loaded thrust stand to a predetermined zero position. Such methods require measurement of the nulling force to equate it to a thrust force. This could include the use of solenoidal force actuators (Rocca and Nicolini, 2005). Other methods include optical position sensing (Grubisic and Gabriel, 2010) and load cells (Gillard et al., 2005). A popular method is that of displacement thrust calibration, which is used in tests of pulsed plasma thrusters (Wilson et al., 1997), Hall thrusters (Polzin et al., 2005), and other thruster types (Moeller and Polzin, 2012). This method relies on an applied set of masses that apply a force in the direction of thrust. These weight (mass times the acceleration due to gravity) increments cause thrust stand movements that are measured using methods such as LVDT (Wilson et al., 1997) (Jamison et al., 2001) and linear gap displacement transducer (LGDT) techniques (Polzin et al., 2005) (Moeller and Polzin, 2012).

The measured displacement from the thruster in operation can be compared to the displacements from the calibration forces (Haag, 1997).

Using the popular applied-weight method requires a calibration system that can overcome friction in its elements and ensure accurate weight addition to the thrust stand in predictable increments. In the CSU thrust stand, a low friction ball bearing with a Teflon outer wheel was used to transfer the force vector from the downward directed weights to a horizontal direction, as shown in Fig. 2-3. Use of an eddy current damper provided reduction of vibrations due to machinery in the vacuum chamber and due to weight addition. The weights were applied using a stepper motor and a linear actuator to ensure steady application of the weights and avoid tangling the weights.

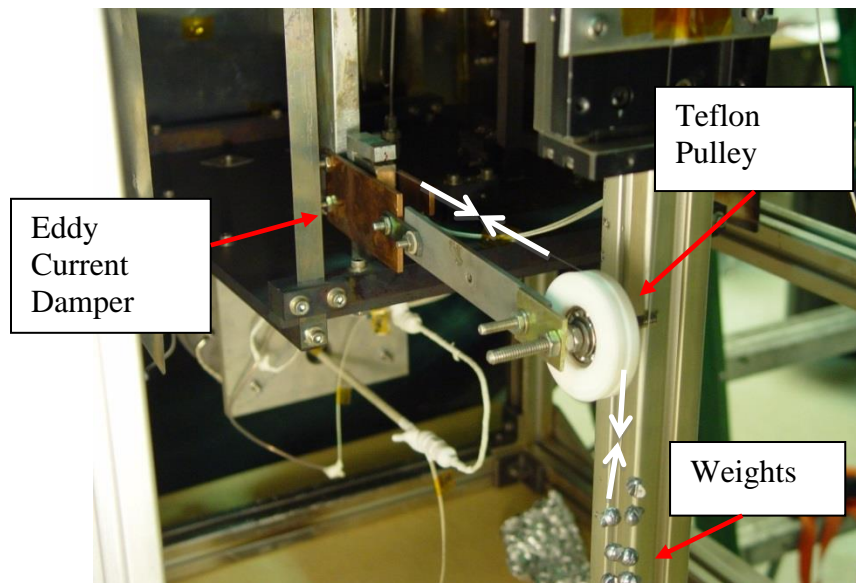


Figure 2-3 Force transfer system for in- vacuum thrust stand calibration. The arrows, which are superimposed over the thin string connecting the weights to the stand, represent force transfer in the calibration system.

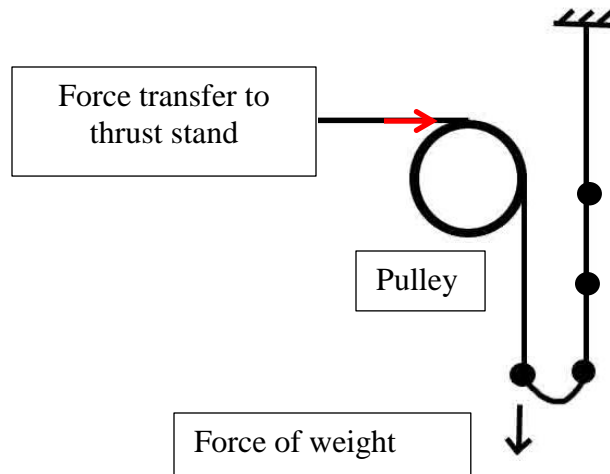


Figure 2-4 Diagram of force transfer in calibration system.

Stepper motor control and data acquisition were both done through a LabView program that commanded the motor to both load and unload weights. Seven on-off cycles of weight addition and removal are shown in Fig. 2-5 in a plot of LVDT signal versus time. The goal behind assigning the program to cycle through weight applications is to determine the repeatability of the system from one cycle of weight addition-removal to the next. It can be seen that after a set of seven cycles at about 100 seconds a cycle there is no visible amount of change between a given weight change from one weight to the next. Limitations in the linear actuators range of motion prevents any more than three weights to be used. Figure 2-6 shows a single weight addition- removal sequence where the force induced by the weights is plotted rather than the LVDT signal.

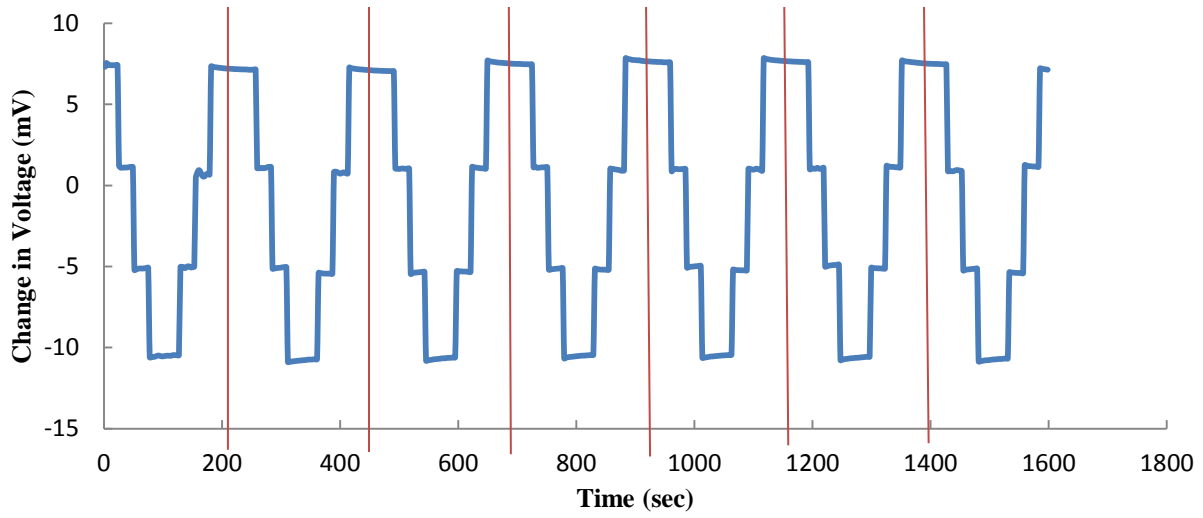


Figure 2-5 Cycles of weight application for calibration.

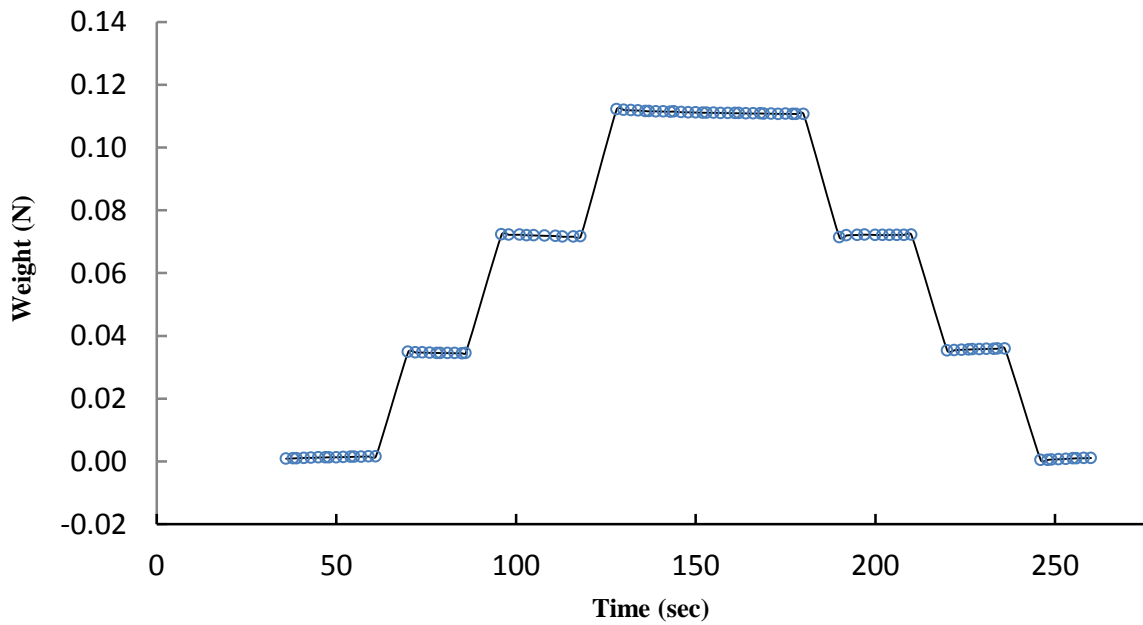


Figure 2-6 One cycle of weights being added and then removed as part of the in-vacuum calibration process.

To increase sensitivity and reduce error, each weight was carefully weighed individually and on a combined whole with the string, to give accurate values for each step in the calibration cycle. Table 2-1 shows the weights that were applied to the thrust stand during an on-off sequence. The LVDT signal was determined by averaging the LVDT signals at each of the steps in the weight addition or removal sequence.

2.6 Determining Sensitivity

The changes in LVDT signal were measured for many weight on-off cycles to determine the sensitivity of the thrust stand. These data are plotted in Figs. 2-7 and 2-8. Figure 2-7 shows the LVDT signal versus the calibration weights along with error bars determined from the standard deviation of the data that were shown in Fig. 2-5.

Table 2-1 List of weight assignments per weight applied in calibration.

Weight combination	Weight total (mN)
1st weight	35.9
1st and 2nd	71.4
1st, 2nd, 3rd	107.4

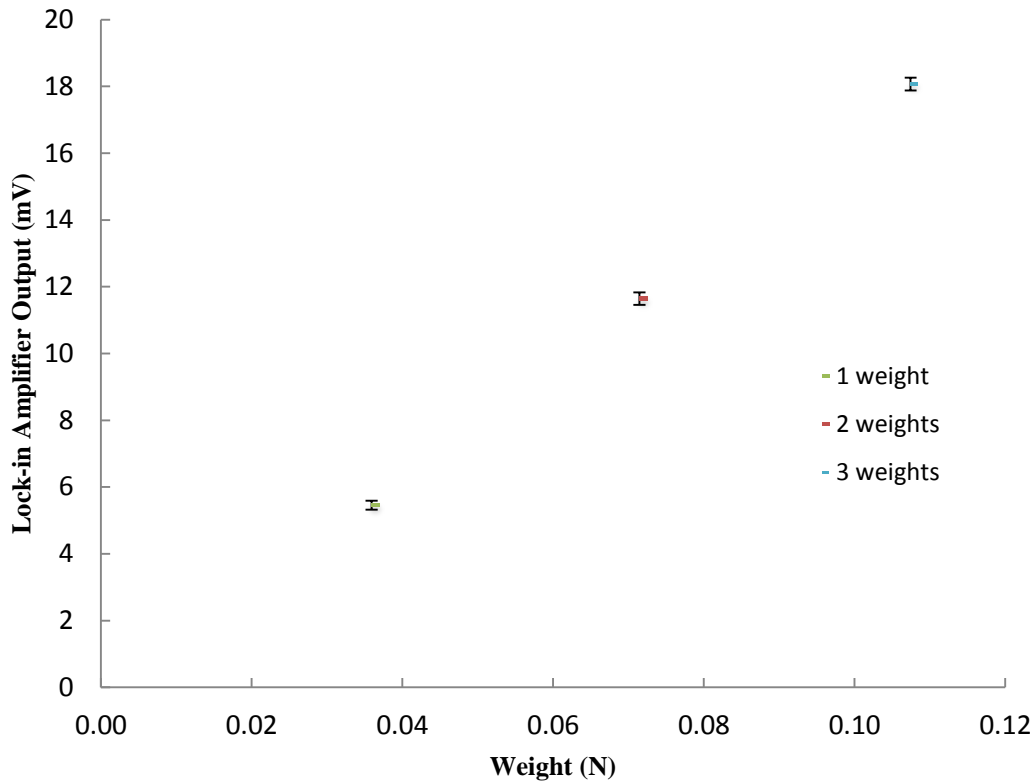


Figure 2-7 LVDT signal for each weight of the calibration process with error bars set to the standard deviation of the LVDT signals.

The error bars show the uncertainty in the LVDT signal at each weight step. The standard deviation in the LVDT signal illustrates the resolution of the thrust stand. For each weight application, a change in voltage of about 5 or 6 mV was registered, whereas the standard deviation between cycles is between 0.137 and 0.191 mV. If the relationship between weight and voltage is considered in the ratio depicted in Eq. (2-1), then the deviation of 0.137 mV equals a change in force application of 0.891 mN for every measurement taken with the thrust stand. The force change derived from the LVDT signal ranges from 0.787 mN to 1.067 mN, which suggests that the target sensitivity range of ± 1 mN was very nearly obtained. A list of all weight changes per step in a typical calibration sequence is shown in Table 2-2. Finally, Fig. 2-8 shows a typical resultant calibration curve that would be used to measure thruster output based on the gathered

data in Figure 2-5. The curve fit equation calculates voltage change (y) as a function of weight change (x).

$$\frac{\text{Force from weight application (mN)}}{\text{Change in voltage (V)}} = \frac{\text{Force sensitivity of stand (mN)}}{\text{Voltage deviation (V)}}$$

(2-1)

Table 2-2 Changes in weight calibration for determining sensitivity of thrust stand.

Weight (mN)	Average Voltage (mV)	StDev (mV)	Change in weight (mN)
35.9	6.18	0.14	0.89
71.4	11.6	0.19	1.20
107.4	18.1	0.19	1.07

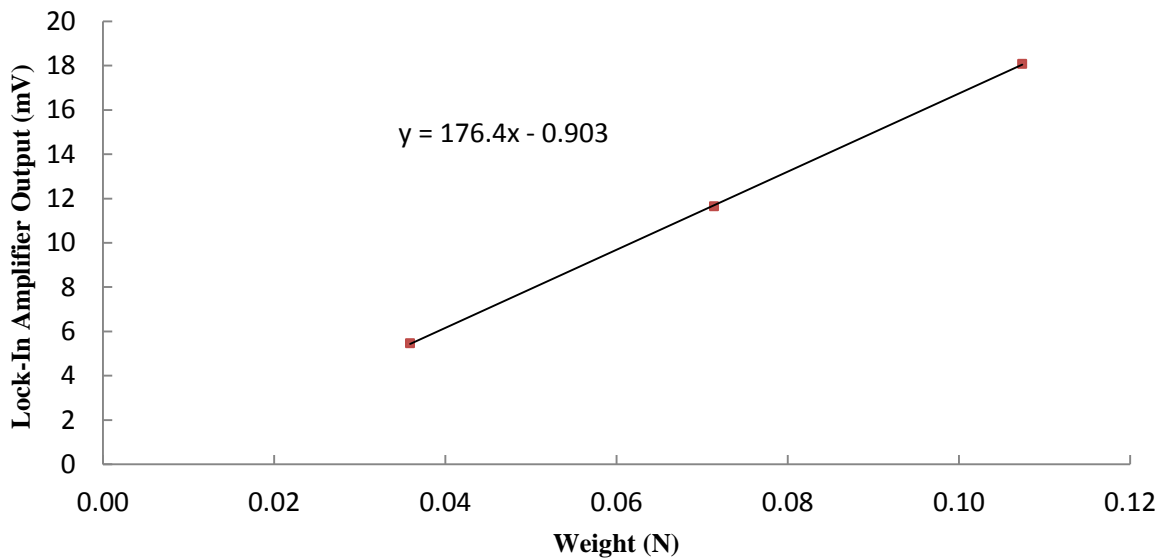


Figure 2-8 Calibration curve gathered from averaging the voltage change per weight added over several cycles.

2.7 Typical Thrust Measurement of CSU Hall Thruster

To test the thrust stand, the CSU laboratory Hall thruster described in Chapter 1 was operated at CSU using xenon gas as the propellant. A calibration data set for the thrust stand was obtained after thruster operation. The vacuum facility used for thruster operation consisted of a 1.7 m diameter by 4.9 m long chamber that was pumped by two 51-cm, 12 kW diffusion pumps. The anode was powered using a 300 V, 3.5 A power supply. A 600 V, 1.7 A power supply was used for biasing the keeper to start the hollow cathode. A 50 V, 12 A power supply was used for the cathode heater. The magnetic poles of the thruster were powered using two Lambda ZUP DC power supplies. As stated in the previous chapter, it was determined that the desired magnetic field within the acceleration channel was obtained when there was 1.5 A of current flowing through the solenoid on the thruster centerline, and 3.5 A of current in the four solenoids that were mounted to the outer pole piece.

The thruster was started and allowed to reach steady-state operation on xenon. Next the thruster was turned ‘on’ and ‘off’ and the changes in LVDT signal were logged. The results of this test are shown in Fig. 2-9. Following the test, the calibration data were collected and they are plotted in Fig. 2-10. The thrust stand LVDT measurement in Fig. 2-9 was used to calculate thrust from the calibration data in Fig. 2-10. Thrust levels ranging from 38.8 mN and 39.3mN were obtained, and the difference of 0.5 mN corresponds to ~1.3%.

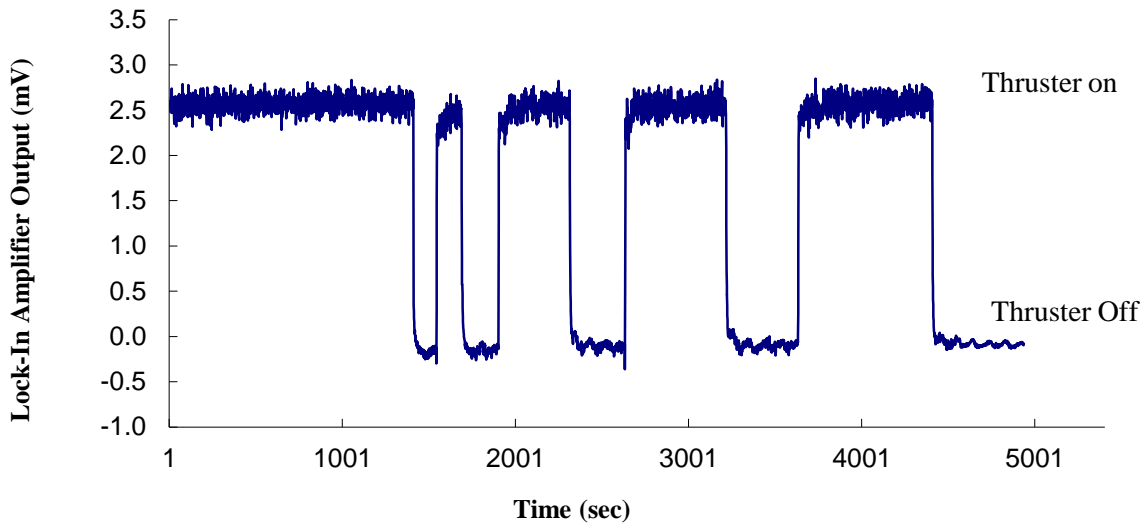


Figure 2-9 LVDT data over a period when the thruster was turned ‘on’ and ‘off’.

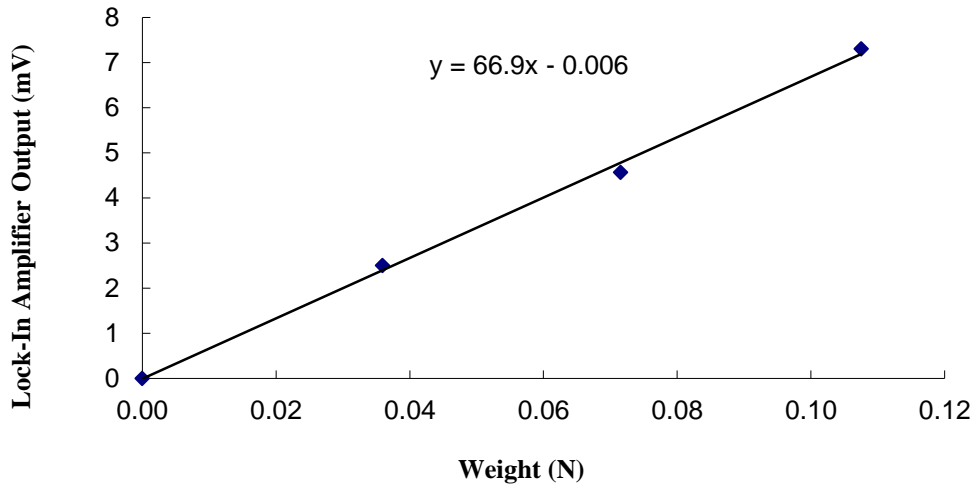


Figure 2-10 Calibration curve with equation of best fit measured after the test in Fig. 2-9 was completed.

The thrust result and corresponding specific impulse and thruster efficiency values were compared against typical Hall thruster performance values reported in Goebel and Katz, (2008), who report that a Hall thruster operating on xenon is expected to have a specific impulse of 1500s to 2000 s and an efficiency of 35% to 60%. The performance of the CSU laboratory

thruster was calculated using the expressions for specific impulse and total efficiency, Eqs. (2-4) and (2-5) from Goebel and Katz, (2008).

$$\eta_T = \frac{1}{2} \frac{\mathcal{T}^2}{\dot{m}_a P_d} \eta_c \eta_o \quad (2-4)$$

$$I_{sp} = (1.037 * 10^6) \frac{\mathcal{T}(N)}{\dot{m}_T(\text{sccm})} \quad (2-5)$$

Where η_T is the total efficiency of the thruster, \mathcal{T} is the thrust (in Newtons), \dot{m}_a is the anode mass flow rate, P_d is the discharge power, η_c is the cathode efficiency, η_o is the electrical utilization efficiency, I_{sp} is the specific impulse, and \dot{m}_T is the total mass flow rate (in standard cubic centimeter per minute, sccm), The efficiency, specific impulse, and thruster operational condition are listed in Table 2-3 and Table 2-4.

It can be noted that the CSU laboratory thruster efficiency and specific impulse are below the efficiency and specific impulse ranges found in the literature for typical Hall thrusters. Although not ideal performance was observed, the results from the test show that the CSU thruster functions and could be used for characterization by magnetic sensor systems in future work.

Table 2-3 Values of operating conditions for the CSU Hall thruster.

Discharge Voltage (V)	Discharge Current (A)	Keeper Voltage (V)	Keeper Current (A)	
300	3.5	16	1.5	
Outer Magnet Voltage (V)	Outer magnet Current (A)	Inner Magnet Voltage (V)	Inner Magnet Current (A)	
10.5	3.5	23.7	1.5	
Discharge power (W)	Keeper power (W)	Magnet power (W)	Mass flow rate Anode (sccm)	
1050	24	72.3	25	
Mass Flow rate Cathode (sccm)	Mass Flow rate Anode (mg/s)	Mass Flow rate Cathode (mg/s)	Cathode efficiency	Electrical efficiency
5	2.5	0.49	0.84	0.92

Table 2-4 Performance of CSU laboratory thruster.

Thrust (mN)	38.8	39.3
Total efficiency (%)	22	22.5
Specific Impulse (s)	1342	1359

3. SIMULATING HALL CURRENT

The focus of this chapter is to present results obtained with a Finite Element Method Magnetics (FEMM) model (Meeker, 2010) on the effect of a simulated Hall current. The goal is to determine if the change in magnetic field, in a selected region nearby the thruster, falls within the sensitivity range of commercially available magnetic sensors.

Based on the work of Haas and Gallimore (1999)(2002) and Thomas et al. (2006), the Hall current is located in a region that begins several millimeters upstream of the exit plane of the Hall thruster and continues up to several centimeters downstream of the exit plane. It is commonly accepted that the peak Hall current axial location is determined by the location of the peak magnetic field in the acceleration channel (Thomas et al., 2006) and the voltage applied between the anode and the exit plane (Raitsev et al., 2003) (Haas and Gallimore, 2002). Most of the cited work associates Hall current location with the location of the acceleration region of the ions where the electric field is the strongest. Haas and Gallimore (2002) further describe the current as being unbalanced across the centerline of the acceleration channel, with a higher current density being located closer to the inner pole piece where the highest magnetic field strength occurs (Haas and Gallimore, 2002). Finally, the axial extent of the region occupied by the Hall current has been shown to be proportional to the discharge current (Haas and Gallimore, 2002).

3.1 Introduction to FEMM

Finite Element Method Magnetics (FEMM) is an open source, 2-dimensional magnetics problem solver. FEMM is capable of axisymmetric problems, in cylindrical and rectangular coordinates (Meeker, 2010). It was used in this thesis to estimate magnetic field magnitude and direction within and nearby a laboratory model Hall thruster. Results were gathered using FEMM's line plot feature, which allows for data to be collected along a selected contour and exported into an Excel file for plotting.

FEMM requires all simulations to be constructed out of a series of lines and nodes that create boundaries representing features being simulated. Property values and input parameters are then assigned to each feature such as material type and current density. The simulation also needs to be surrounded by a boundary, which was selected to be 130 times greater than the Hall thruster volume to avoid boundary edge-induced errors and ensure that an accurate simulation was performed in the regions nearby the thruster. In the simulations conducted for the laboratory thruster model, air was used as the material type surrounding the thruster and within voids. It should be noted that the permittivity of air is the same as that of a vacuum, where the Hall thruster is actually operated.

The model thruster was simulated using 1018 steel for the thruster body and copper with a specified current density for the coil magnets as shown in Fig. 3-1. For a center coil with 100 wire turns, using a wire diameter of 0.07 cm and an applied current of 1.5 A, the current density was calculated to be 1.3 MA/m^2 using the relationship shown in Eq. (3-1)

$$density = \frac{(N)(I_{coil})}{(A_{coil})} \quad . \quad (3-1)$$

Where N is the number of coil turns, I_{coil} is the applied current, and A_{coil} is the coil cross sectional area.

Due to the axisymmetric nature of the FEMM simulation, the outer pole piece needed to be modeled with two symmetrical outer coils that represent the four individual coils used to magnetize the outer pole piece. The two axisymmetric outer coils in the FEMM model were selected to have areas and current density that produced the same magnetic field as the four coils in the laboratory thruster. The current density is calculated using Eq. (3-1) and 3.5 A as the applied current, I_{Coil} , in the wires of the outer coils. Current direction in a coil specifies the sign associated with the current density value and a negative current density implies current coming out of the page while positive current density implies current going into the page. The current density direction in the inner and outer coils determines the direction of the magnetic field in the channel and hence the electron drift in the thruster. Figure 3-1 illustrates the FEMM model layout, and depicts the location where Hall current would be simulated. The area for Hall current was selected to be larger than the channel width of the actual thruster when including the presence of the ceramic Borosil channel lining. Since the ceramic material does not have an effect on the magnetic field of the thruster, it was neglected in the FEMM model. The simulation of Hall current used herein cannot be considered exact, and is instead only representative of the actual Hall current. The area of examination for magnetic sensor placement was selected to expand well into the thruster plume and far beyond the outer radius.

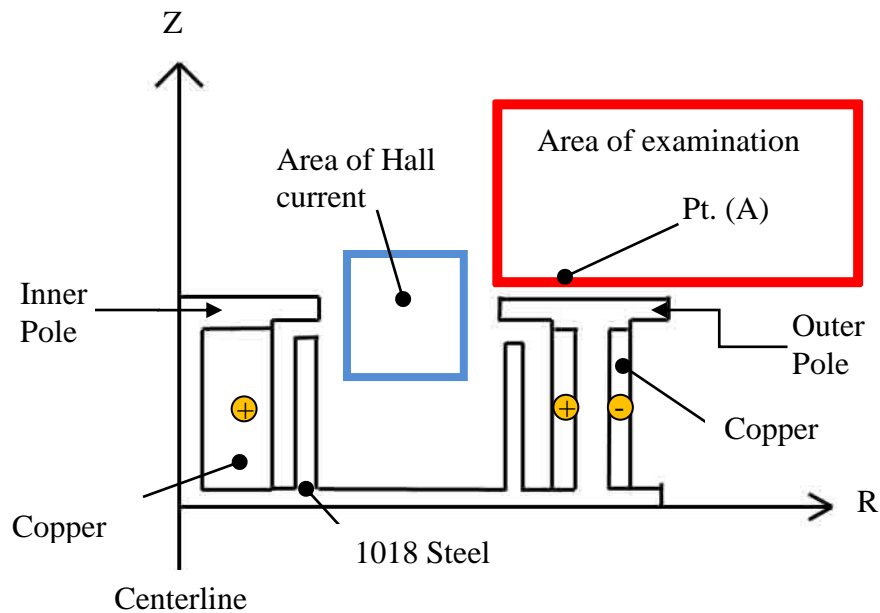


Figure 3-1 FEMM Axisymmetric Model of SPT100 Thruster. The red box indicates the area where magnetic field data were collected. The blue box shows the area where simulated Hall currents were placed. The + and – signs depict the direction of applied coil current.

3.2 Hall Current Simulation

It was decided that Hall current simulations will be performed on three different configurations, to investigate Hall current density effects on magnetic field change above the outer pole piece.

The objectives include:

1. Does Hall current, when distributed uniformly or discretely over a given region, cause detectably different magnetic fields in test sensor locations?

2. Can unbalanced Hall current about the channel centerline cause magnetic field changes that are detectable at test sensor locations?

3.2.1 Objective 1 Investigation

To address Objective 1, four comparable geometries were used to represent the Hall current distribution in FEMM, and the results of the magnetic field strength changes above the outer pole piece were compared. The CSU laboratory thruster was designed to operate at a discharge current of $\sim 3.3\text{A}$. Rubin et al. (2004) suggest that the Hall current is between 3 to 15 times larger than the discharge current, and it was decided on this basis that a minimum Hall current of 10.5 A and a maximum of 75A would be used in FEMM simulations.

The Hall current configurations selected to investigate Objective 1 are shown in Fig. 3-2 and Fig. 3-3. The first configuration in Fig. 3-2 consists of a circular region in the acceleration channel where the Hall current is uniformly distributed. Two different circular diameters were investigated. The second configuration used to investigate Objective 1 is illustrated in Fig. 3-3 and consists of a cluster of small diameter (0.127cm) “wires” arranged in a circular ring. Hall current density is distributed evenly amongst the wires to produce the same total Hall current as shown in Fig. 3-2 . Two different ring diameters were investigated.

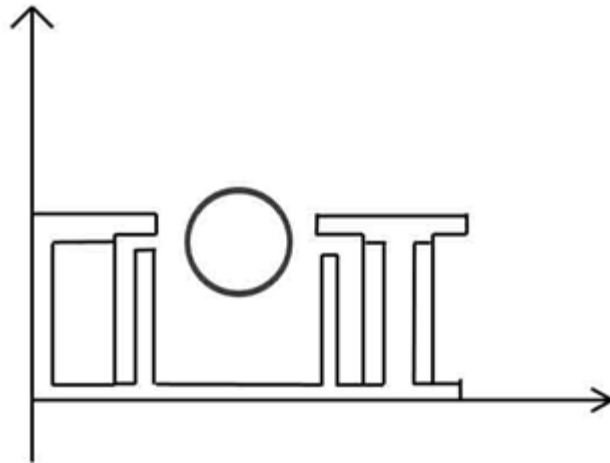


Figure 3-2 Hall current cross section simulated with a 2.54 cm diameter symmetrical section located near the acceleration region of the thruster. In this figure, Configuration “B” is shown. Configuration “A” is the same but with a 1.27 cm diameter section.

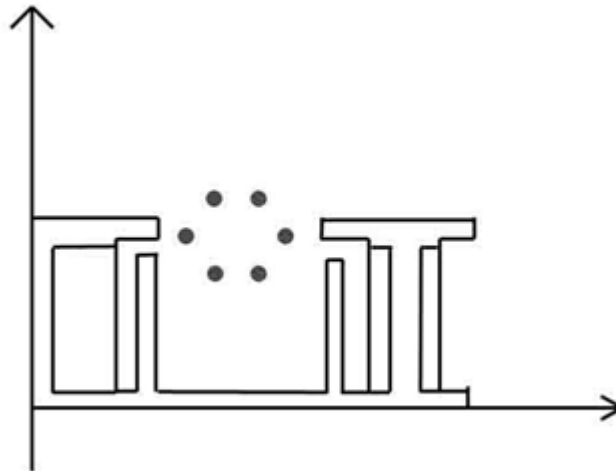


Figure 3-3 Hall current cross section modeled using 6 small, 0.127 cm diameter "wires" of current spaced equally around a 2.54 cm circle that was located near the acceleration region of the thruster. In this figure, Configuration “D” is shown. Configuration “C” is the same only with a 1.27 cm ring diameter

Placement for the Hall current was chosen based on the location of maximum applied magnetic field calculated using FEMM simulations and magnetic mapping measurements of the actual thruster. This position is in general agreement with the work done in Haas and Gallimore

(2002) and Thomas et al. (2006). Results were gathered over the region above the outer pole piece as shown in Fig. 3-1. Hall current was created in each configuration by assigning air a specific current density based on the desired level of Hall current and the cross sectional area of the simulated current. This created significantly higher current densities in the “small wire” configurations than in the large circular configuration. For the configuration involving small wires, the selected Hall current was first divided by the number of wires and then converted to a density using the cross sectional area of an individual wire. Current direction was determined based on the direction of the applied magnetic and electric fields.

To simulate a thruster in “off position” a FEMM simulation was run with only the magnetic field provided by the magnet coils, and no simulated Hall current applied. A baseline set of data was taken from this simulation, and was used to compare to every other test. A total of eight simulations with Hall current were performed and compared to a scenario where the Hall current was “off”. The maximum magnetic field change due to the Hall current for each simulation was recorded. In addition to determining the maximum change in magnetic field, each scenario was compared to another scenario to determine whether different Hall current configurations produced different results. Table 3-1 summarizes the comparisons that were made between simulations. Most magnetic field changes between the thruster “on” and the thruster “off” condition were found to be in the 2.5-3.5 Gauss range. The magnetic field strength changes between configurations were found to be in the 0.002 to 0.05 Gauss range. Figure 3-4 shows a contour plot of the change in magnetic field when the Hall current is increased to 75 A from the “off” condition for Configuration “D”.

Table 3-1 List of Hall current distribution comparisons. All distributions were tested at 10.5 A and 75 A Hall current and compared to a state where the thruster is considered “off” and without Hall current. This table provides a sample of magnetic field strength from the 75 A tests, at a sensor location positioned at R=7.11 cm, Z=5.58 cm over the outer pole piece.

Condition	Vs.	Condition	$ \Delta B $
1.27 cm diameter Configuration A	Vs.	2.54 cm diameter Configuration B	0.054 Gauss
1.27 cm diameter Configuration A	Vs.	1.27 cm ring Configuration C	0.049 Gauss
2.54 cm diameter Configuration B	Vs.	2.54 cm ring Configuration D	0.002 Gauss
Configuration A	Vs.	off	3.34 Gauss
Configuration B	Vs.	off	2.80 Gauss
Configuration C	Vs.	off	2.84 Gauss
Configuration D	Vs.	off	2.78 Gauss

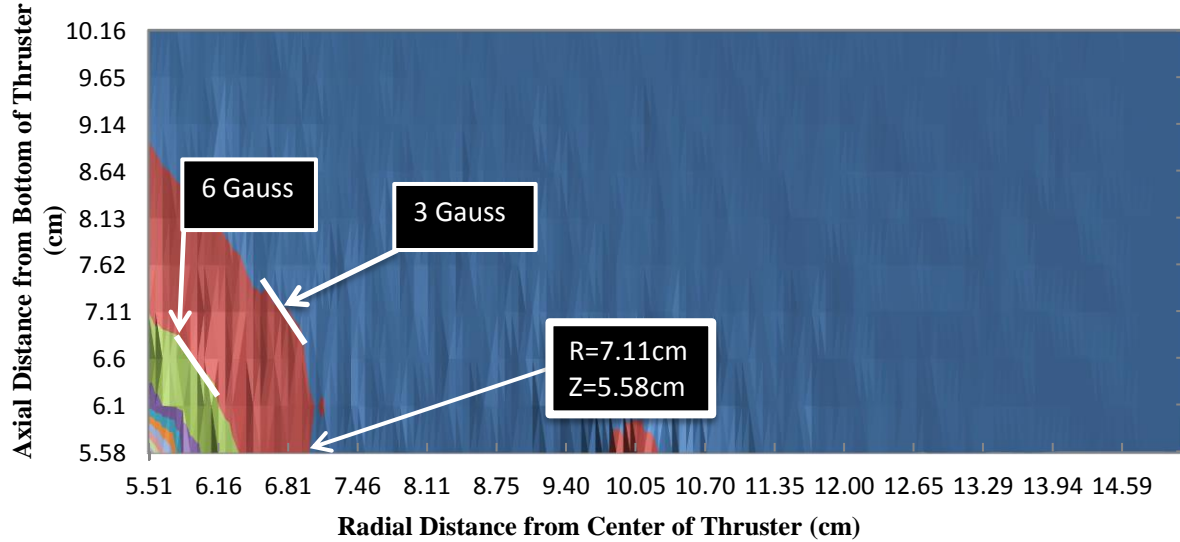


Figure 3-4 Contour plot of magnetic field strength change between “Configuration D” with Hall current at 75 A, and the same thruster with zero Hall current, otherwise known as the “off” condition. Contour color changes are at an equal spacing of 3 Gauss.

If the above scenario is examined near the separatrix² on the outer pole piece, which is near the R=7.11 cm location, a maximum magnetic field change would be about 0.0003 Tesla or 3 Gauss. There is also a noticeable change in magnetic field at a location near the inner and outer edge of the outer pole piece, which was prominent in every simulation that was conducted. It can be noted that in each simulation, similar distributions of magnetic field change were produced. The lowest change occurred with the first simulation, which compared the “off” thruster to a 1.27 cm diameter low density model running at 10.5 A. The results of that test produced a magnetic field change of only about 1 Gauss. A point of measurement, Pt. A in Fig. 3-1, for comparison in this thesis is located 7.11 cm radially outward from the center of the thruster and at a height of 0.19 cm (Z=5.58 cm) above the surface of the outer pole piece.

² The magnetic field separatrix is a surface which divides the magnetic field into internal and external regions, and has been suggested to be a possible location for cathode placement (Sommerville and King, 2011)

Figure 3-5 shows the difference in magnetic field produced from the ring of “wires” (Configuration D) to a similar test with Configuration B. It can be seen in this plot that there is a difference between these two scenarios, both operated at 75A Hall current, however, the maximum difference found is only half a Gauss. It is left to debate whether this is a significant enough difference to be detected above the existing background field.

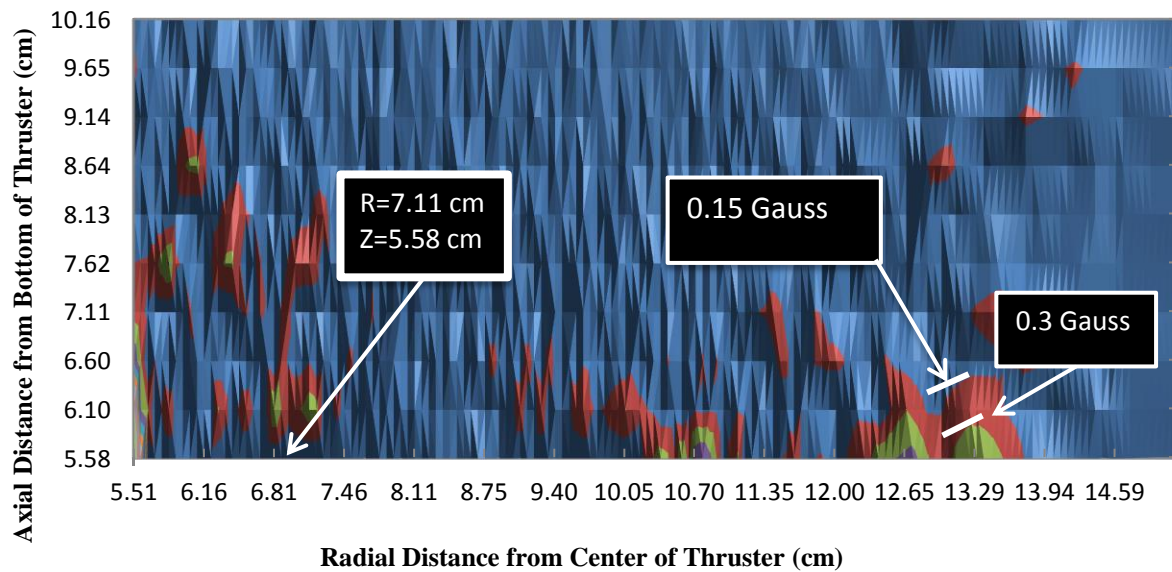


Figure 3-5 Difference in magnetic field magnitude between “Configuration D” and “Configuration B” at 75 Amps Hall current. Contour lines represent equal spacing of 0.15 Gauss.

3.2.2 Objective 2 Investigation

Based on the work done by Haas and Gallimore (2002), Thomas et al. (2006), and Raitsets et al. (2002), a Hall current configuration was investigated that emphasized the unbalanced or asymmetrical quality of the Hall current about the centerline of the channel. As shown in Fig. 3-6, two points were used to represent the Hall current. The “wire” setup was used because a different

current density could be applied to each wire. Placement for the wires was based on Thomas et al. (2006), where it was indicated that the Hall current occupied an oval shaped area near the exit plane of the thruster. The wires were axially located at the downstream edge of the acceleration region at $Z=5.58$ cm, or 0.19 cm above the exit plane, and 2.54 cm apart from each other. Three tests were performed, each at 75 A Hall current. First, each wire had equal current density applied, and the results were compared to the thruster “off” state. A second simulation was run where wire “B” had 75% of the current, and wire “A” was reduced to 25%. In the final test, the unbalanced Hall current values were reversed. Data were compared along the $R=7.11$ cm, and $Z=5.58$ cm directions as shown in Fig. 3-6. The results of these comparisons are shown in Figs. 3-7 and 3-8. Figure 3-7 displays a plot comparing the results from each simulation.

It was determined that the field increase around the $R=5.8$ and $R=10.2$ cm location (locations 1 and 2 in Fig. 3-7) is a result of rapid field direction change due to the geometry of the coils and pole piece. Field change at $R=10.2$ cm (location 2) is minimal, and does not provide enough change in the field for a sensor. The high field change present at $R=5.8$ cm (location 1) would be easily detectable by a sensor, however, it is located in the thruster plume and therefore, not an ideal location. This leaves the range identified at location 3, which displays a measurable magnetic field change, and a habitable environment for a sensor. The peak magnetic field around the $R=7.11$ cm location near the surface is just under 50 Gauss, and the applied Hall current decreases the field proportional to the Hall current density and location. As an interesting aside, Thomas et al. (2006) found that the Hall current decreased the peak magnetic field in the channel of the thruster by up to 15%. Location 3 results are used in Chapter 4 to determine if existing magnetic field sensors can be used to measure field changes in this range.

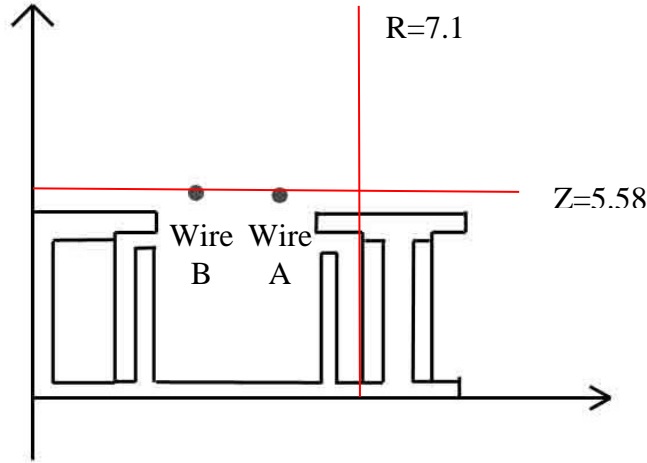


Figure 3-6 The red lines indicate where magnetic field magnitude data were taken for each test. The horizontal line is located at $Z=5.58$ cm or 0.19 cm above exit plane. The vertical red line is taken at $R=7.11$ cm. It is noted that a position along $R=7.11$ cm between 0 and 1 cm above the pole piece would be a good sensor location.

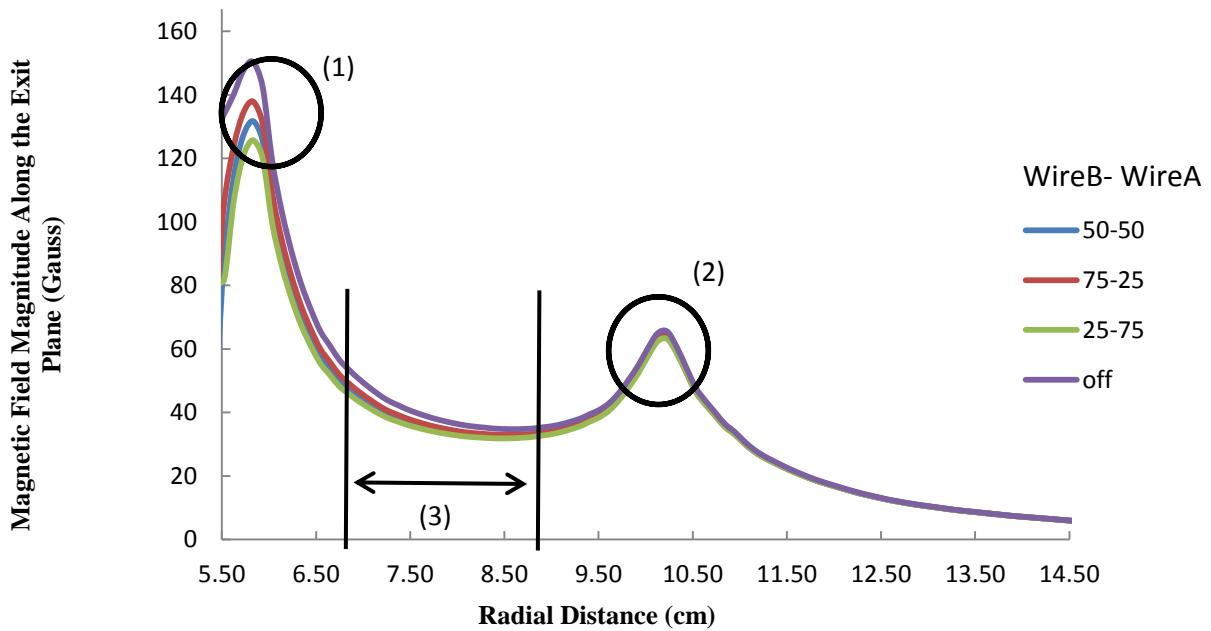


Figure 3-7 plot of Magnetic field magnitude along the exit plane of the thruster for three cases of Hall current simulation.

Figure 3-8 shows the magnetic field along the $R=7.11$ cm line. Again the magnetic field decreases when Hall current is present as expected. The simulation with equal amounts of Hall current distribution falls almost exactly between the cases of unbalanced distribution. The 25-75% split configuration, where the higher Hall current would be closer to the sensor location, causes the largest decrease in magnetic field at the sensor location. Based on the work of Haas and Gallimore (2002), however, it was stated that the area of highest Hall current concentration would be located nearest to the center pole. Therefore the 75-25% distribution, with higher Hall current density located furthest from the sensor location, would be the most accurate representation of Hall current in FEMM out of the previously listed configurations. Figure 3-8 illustrates that the magnetic field change in the 75-25% simulation, while the smallest change out of all the simulations, is large enough for detection by a magnetic field sensor as discussed in Chapter 4.

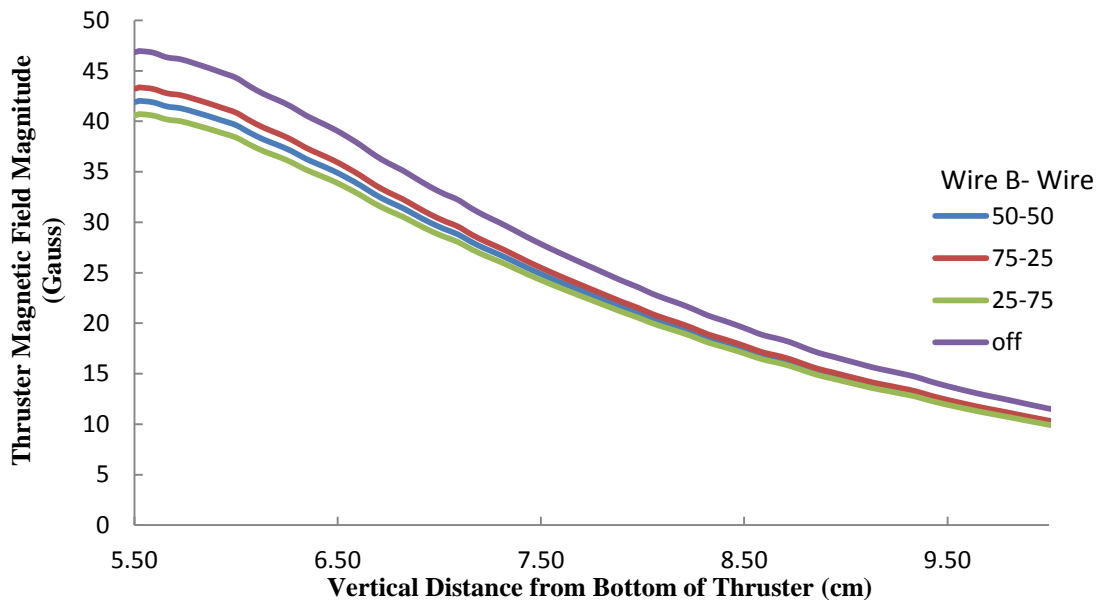


Figure 3-8 Plot of the magnitude of magnetic field along the $R= 7.11$ cm line for all three simulations of Hall current distribution, compared to the thruster “off” simulation.

3.3 Sensor Positioning Based on FEMM Analysis

The preferred sensor position and orientation on a Hall thruster is at the location of the largest magnetic field change while still remaining free from the thruster plume, which could damage the sensor and inhibit thruster performance. As described earlier, the FEMM software was used to calculate the radial and axial components of the magnetic field created nearby the outer pole piece. Magnetic field results from FEMM can be output as the magnitude, or as tangential and normal components with respect to a selected contour. For the previously discussed simulations, data were collected for each category (magnitude, tangential, and normal) for conditions of Hall current applied, and no Hall current. The normal components of magnetic field with respect to selected contours are plotted in Figs. 3-9, 3-10, 3-11, and 3-12. The two contours used are the same as used in the previous tests ($Z=5.58$ cm and $R= 7.11$ cm). Figures 3-9 and 3-10 show the magnetic field components in the axial and radial directions, respectively, when Hall current is present. Figures 3-11 and 3-12 show the change in magnetic field in each orientation between conditions where simulated Hall current is “on” and when it is “off”. For these tests the maximum Hall current of 75 total Amps was used.

The results depicted in Figs. 3-11 and 3-12 suggest a region constrained by $6.6\text{cm} < R < 8.6\text{cm}$ and $5.5\text{cm} < Z < 6.5\text{cm}$, where non-contact sensors could be placed. Although both radial and axial fields will need to be sensed, the axial field change is larger and would be easier to measure. The capability of commercially available magnetic sensors is discussed in the following chapter.

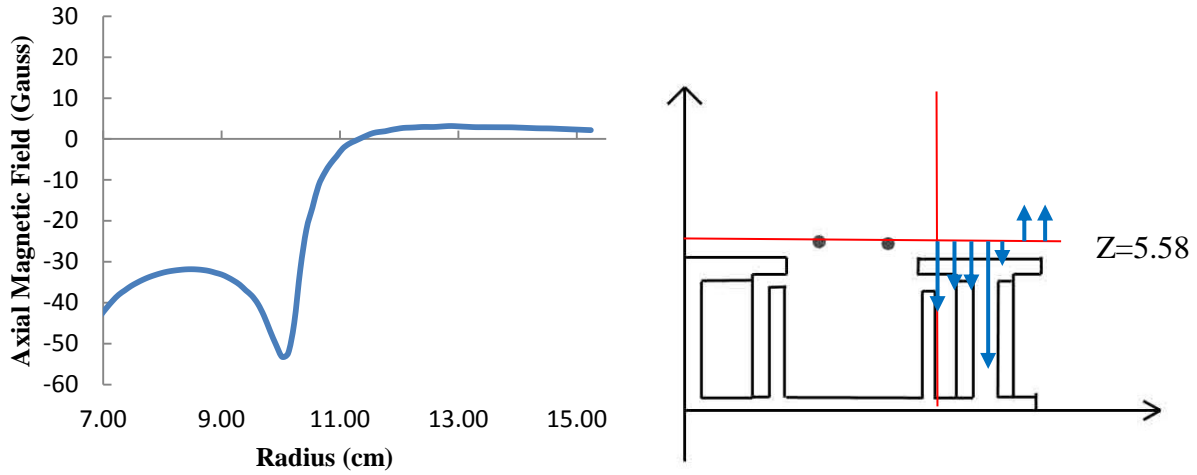


Figure 3-9 Axial magnetic field along the $Z=5.58$ cm contour (with applied Hall current). Arrows on the figure illustrate field component that is plotted.

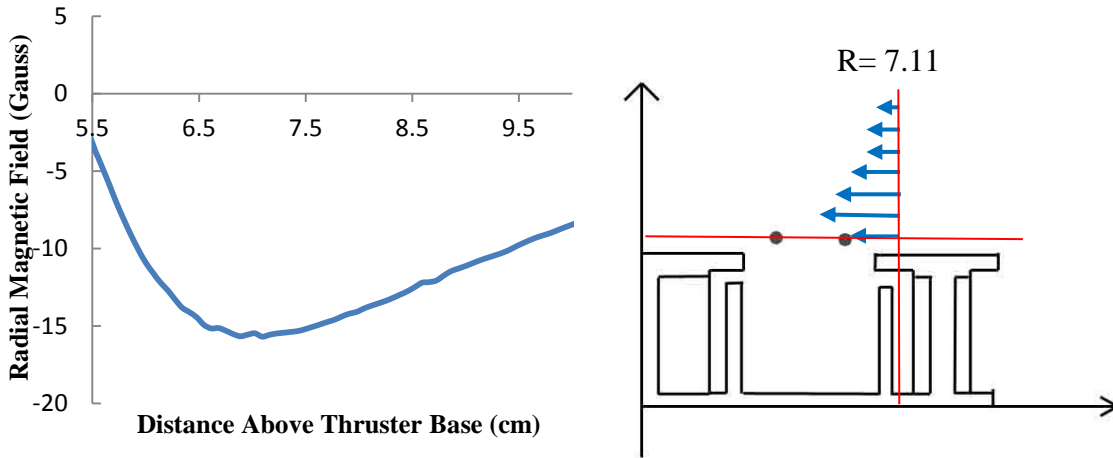


Figure 3-10 Radial magnetic field along the $R=7.112$ cm contour (with applied Hall current). Arrows on the figure illustrate field component that is plotted.

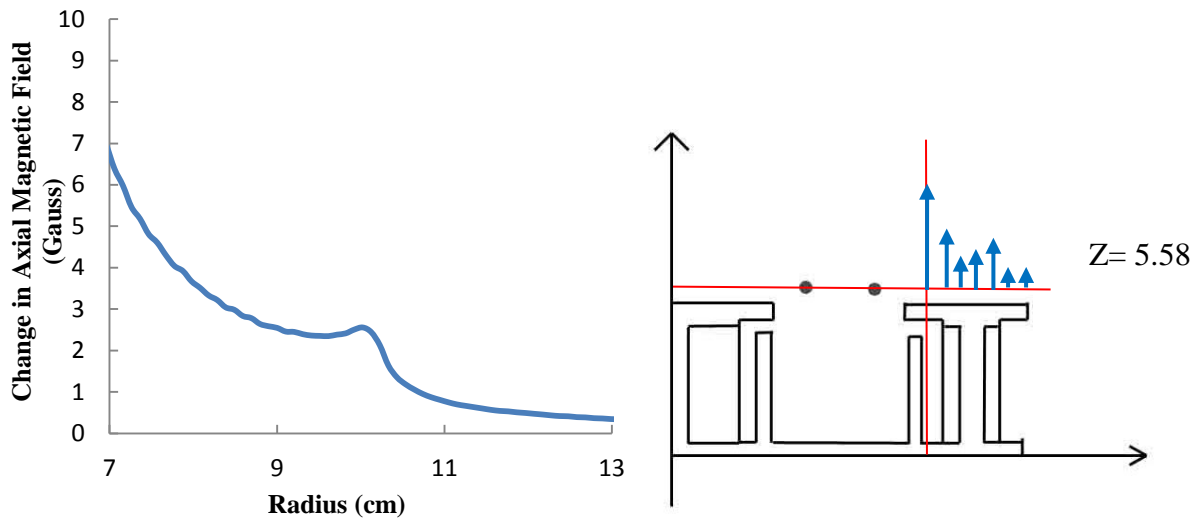


Figure 3-11 Change in axial magnetic field along the $z=5.58$ cm contour (with 75 A total Hall current in the configuration with 50/50% current split).

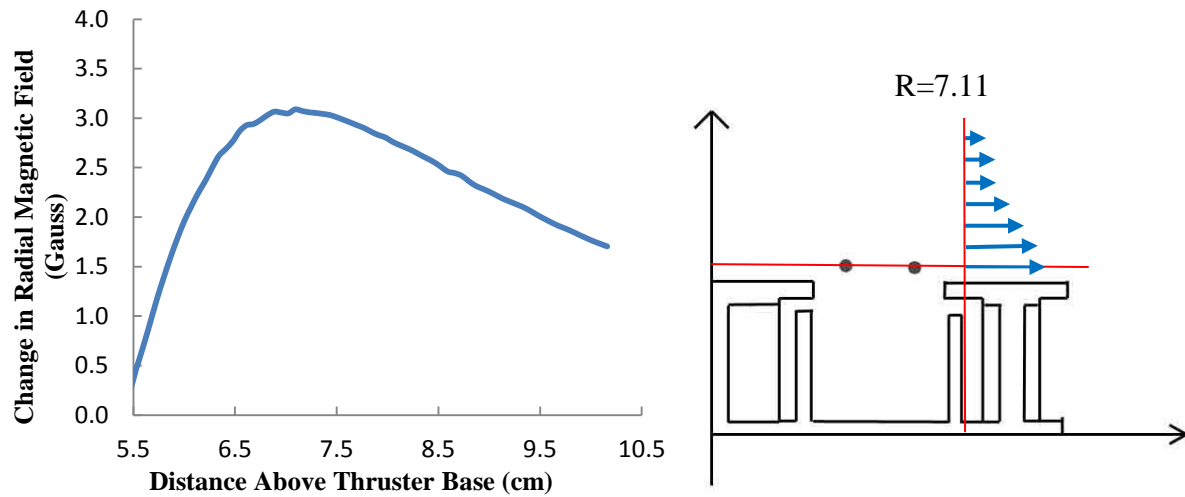


Figure 3-12 Change in radial magnetic field along at the $r=7.112$ cm contour (with 75 A total Hall current in the configuration with 50/50% current split).

4. MAGNETIC SENSORS

Many sensors are available to measure magnetic fields, and each sensor type has advantages and disadvantages. If a sensor is to be placed nearby a Hall thruster, it needs to survive relatively high temperatures and be sensitive enough to detect small changes in a high static background magnetic field. In addition, a useful sensor must be small, consume little to no power, and have an easily conditioned output signal. The magnetoresistive class of sensors meets these requirements. This chapter presents the concept behind the operation of magnetoresistive sensors, and how they may be applied to measure the magnetic field induced by the Hall current of a Hall thruster in operation. The following sections contain:

- 1) Background on anisotropic magnetoresistive (AMR) and giant magnetoresistive (GMR) sensors.
- 2) Sensor experimentation results of magnetic fields created by flowing current in a wire.
- 3) Sensor experimentation with a constant background magnetic field and with current flowing in single and multiple wires.

The results obtained in this chapter will be compared to the FEMM simulations that were presented in Chapter 3. These results are used to determine if commercially available sensors possess the sensitivity to measure magnetic field changes caused by the Hall current in a 1kW laboratory Hall thruster.

4.1 Magnetoresistive Sensors

An anisotropic magnetoresistive (AMR) sensor can be explained using the Corbino disk. The Corbino disk, as shown in Fig. 4-1, was first investigated in the early 1900s (Kleinman and Schawlow, 1960)). A pair of concentric, electrically conductive rings, are connected by conducting media, with the center ring connected to a positive bias and the outer ring connected to a negative bias. Under conditions where no magnetic field exists, current will travel in a direct path from the inner ring to the outer ring. When a magnetic field is applied parallel to the axis of the rings, it will distort the current path so it spirals outward and follows a longer path (Kleinman and Schawlow, et al., 1960). This spiraling of the current is an example of the Hall effect, which was previously discussed in the first chapter.

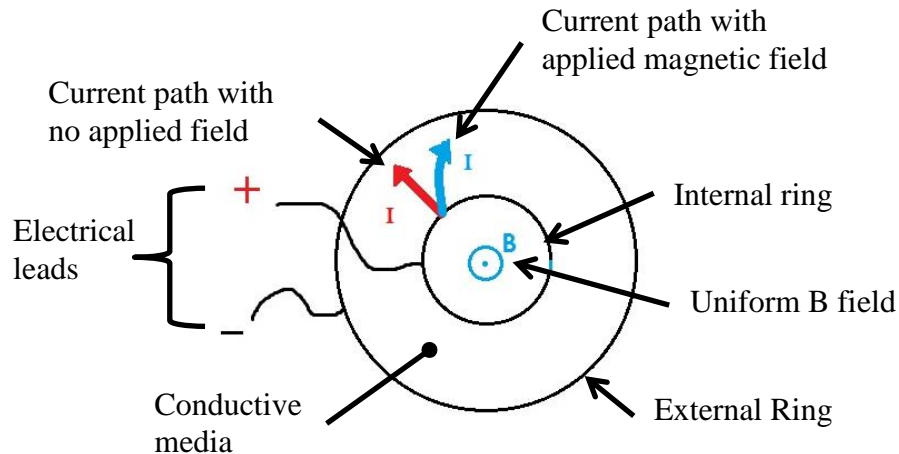


Figure 4-1 Corbino disk illustrating anisotropic magnetoresistance (AMR).

The effective resistance of the conductive media increases with magnetic field due to the lengthened current path and a fixed current flowing through the conductive media will induce a larger voltage that is indicative of the magnetic field. A magnetoresistive sensor works through this same principle and is illustrated in Fig. 4-2. A current applied by biasing the “+” and “-” terminals creates the axis of sensitivity (the direction of magnetic field that may be measured), which lies perpendicular to the plane of the sensor. When exposed to a magnetic field, the

current path length increases, which increases the voltage measured across the sensor between measurement points A and B (Caruso et Al., 1998).

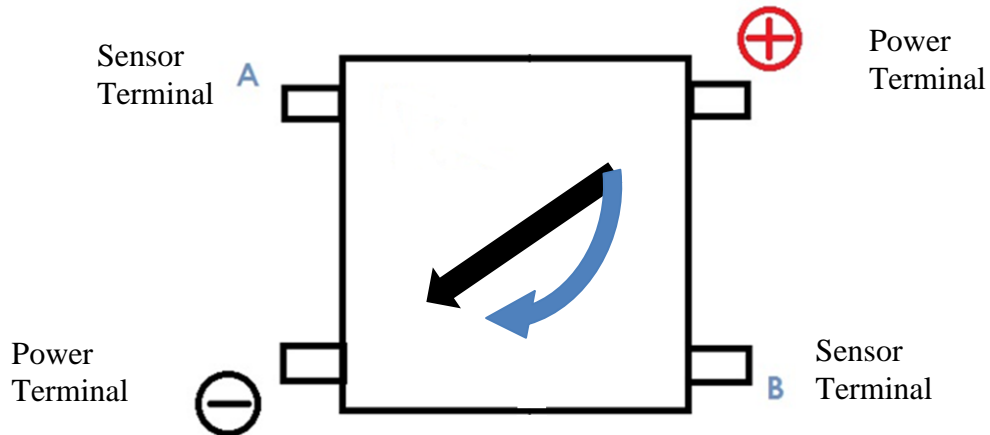


Figure 4-2 Changing path of current in a magnetoresistive sensor, when magnetic field is applied. The new path is signified by the blue arrow, while the original path (with no applied magnetic field) is shown by the black outlined arrow. The B-field detection direction is the same as in the Corbino disk.

Unfortunately, AMR sensors have sensitivity limitations when used in environments containing large background magnetic fields above ~ 1 Gauss (Caruso et al., 1998)(Popovic et al., 2002). Giant magnetoresistive sensors (GMR) work through an entirely different principle and do not suffer from the same limitation, allowing them to measure changes in magnetic fields at higher static background field levels. GMR elements consist of three layers of material that vary between thicknesses of 15 \AA and 18 \mu m based on the desired application (NVE 2012). The top and bottom layers are made from a ferromagnetic material. When two pieces of ferromagnetic material are positioned within nanometers of one another with no outside influences (such as external magnetic fields), their electron spin directions will oppose one another due to antiferromagnetic coupling (NVE, 2012). The material in the middle layer of a GMR element is non-magnetic and electrically conductive. Materials that are traditionally good conductors at

macroscopic scale often behave very different when scaled down to the nanometer level. As a current is conducted along the plane of the nanometer thick conductive layer, the conduction electrons have a much higher probability of being scattered off of other electrons and off the top and bottom boundaries (interfaces) of the conductive layer. As a result, the resistivity of the conductive material is much higher than a thicker sample made from the same material. The exact value of resistivity is dependent on the spins of the other electrons in the GMR element. If the spins are mixed, the scattering probability (and thus the resistance of the GMR element) increases. When the GMR sensor element is not exposed to an external magnetic field, the electron spin directions are random and the spins in the two ferromagnetic layers are anti-symmetric, leading to a mix of spin directions in the conductive layer and a higher resistance. If the sensor is placed in a sufficiently strong magnetic field, the spins in the ferromagnetic layers will align with the magnetic field (and as a result, one another), causing the spins in the conductive layer to align, which leads to less frequent scattering and a lower resistance (NVE, 2012) (Caruso et Al., 1998). An illustration of this process is shown in Fig. 4-3.

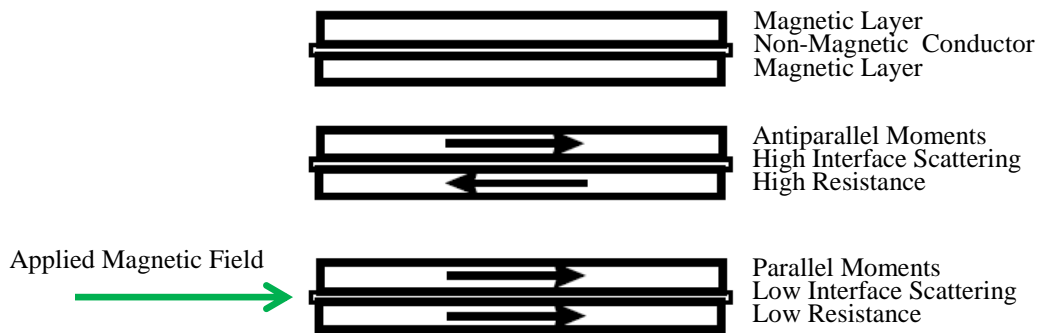


Figure 4-3 Layers of material in GMR elements (Caruso et al., 1998).

A GMR sensor is typically laid out in a Wheatstone bridge configuration, where two fixed resistors are placed in series with two GMR elements, which are then placed in parallel

with each other as shown in Fig. 4-4. Sensor operation requires a constant voltage to be applied across the bridge. The induced voltage is measured to determine the applied magnetic field.

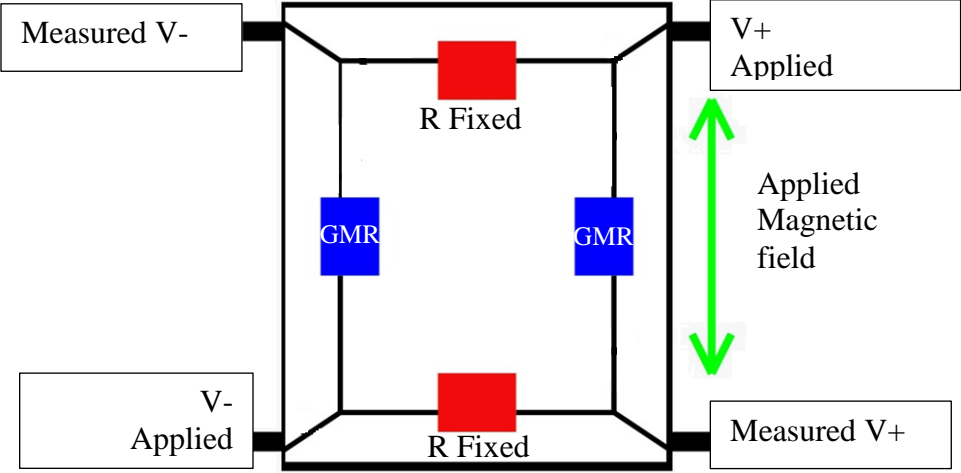


Figure 4-4 A diagram of the inside of a GMR magnetic sensor. The red resistors are fixed, and the blue resistors are made from the nano layered GMR material. The green arrows designate the direction of the magnetic field to be measured.

Similar to an AMR sensor, GMR sensors have a single axis of sensitivity along which a magnetic field may be measured. Figure 4-5 shows a GMR sensor being used to sense the magnetic field created around a wire carrying a specified current. The magnetic field is in the plane of the sensor as is also shown in Figs. 4-3 and 4-4.

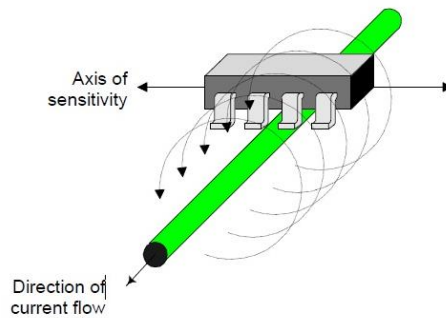


Figure 4-5 Axis of sensitivity provided by NVE Corporation GMR sensors (NVE, 2012).

Based on the results of magnetic field mapping of the laboratory thruster using a Gaussmeter, and the FEMM calculations, it was determined that a sensor would be exposed to a maximum magnetic field of ~ 70 Gauss and a minimum field of ~ 6 Gauss in the region above the outer pole piece identified in Chapter 3. To produce meaningful results, a sensor employed on an operating Hall thruster would need to register a change in magnetic field strength as small as ~ 0.5 Gauss with a resolution of $\sim 1\%$. Based on these numbers the AA005-02 sensor from NVE Corporation was chosen. It has a linear range of 10 to 70 Gauss in air with a sensitivity of 0.45-0.65 mV/V/Gauss. A second sensor, the AA002-02, was also evaluated and it has a lower measurement range of 1.5 to 10.5 Gauss in air, and a higher sensitivity of 3.0-4.2 mV/V/Gauss. The second sensor was used for measuring the magnetic field induced by currents that were flowed through a single, thin wire. These measurements were used to verify the sensitivity published by the NVE Corporation.

4.2 Experimental Design and Validation

An experimental setup similar to Fig.4-5 was used to characterize a GMR sensor using a current flowing through a long straight wire. Sensor placement relative to the wire was varied. This was done using a support arm attached to a linear actuator whose direction of travel allowed

the sensor to be moved radially away from the wire. The wire was strung horizontally and the sensor was positioned on the arm in a direction that aligned its axis of sensitivity with the magnetic field at that point. The wire supports and the support arm were fabricated from teflon to electrically insulate the wire and sensor power leads and eliminate stray magnetic fields at the test location. This apparatus is shown in a photograph in Fig. 4-6, and in an illustration in Fig. 4-7.

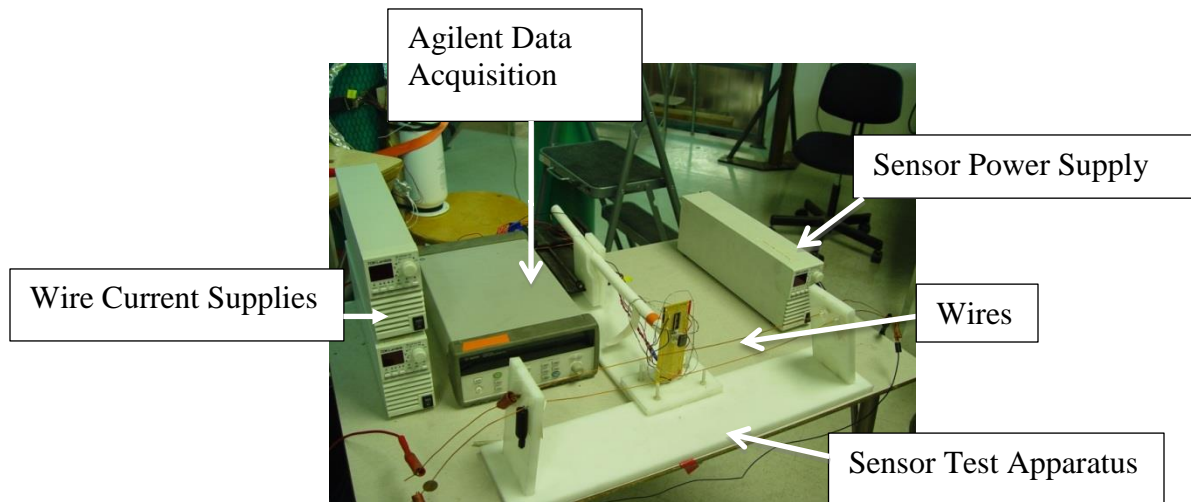


Figure 4-6 Experimental facility for sensor testing.

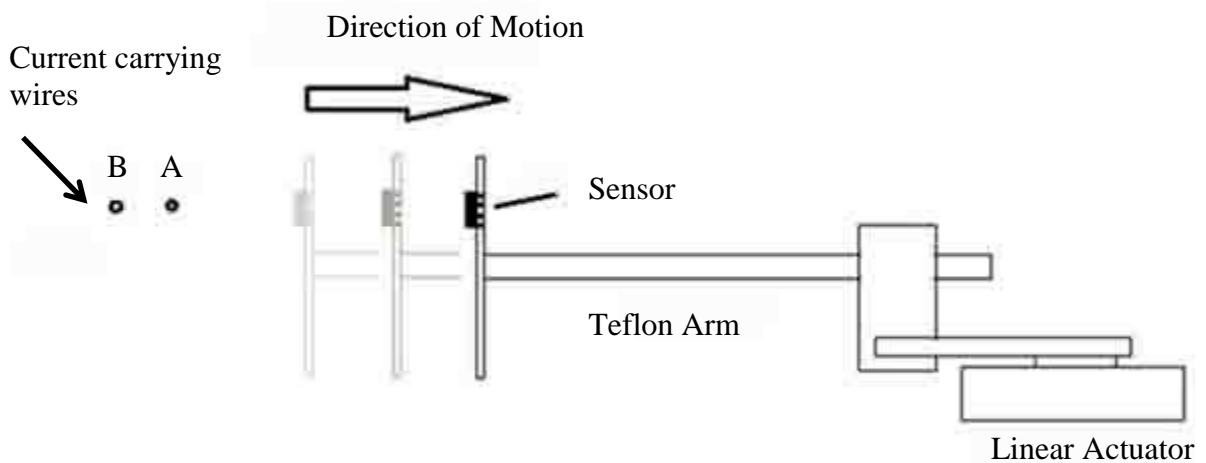


Figure 4-7 Direction of motion of sensor relative to wires A and B.

Figure 4-6 shows two parallel wires that were used to re-create the dual “wire” FEMM simulations in Chapter 3. Only one wire was used for the testing described in this section. Three power sources were required to provide current to both wires and power to the sensor. Data were collected using an Agilent multimeter and data acquisition system. The sensor was mounted in a chip carrier on a breadboard that allowed for easy installation and removal of sensors.

Validation of the experiment design was done by installing the lower range sensor, the AA002-02, using current applied to a single stainless steel wire. An input voltage of 8.6 V was applied to the sensor. As shown in Fig. 4-7, the sensor was moved radially away from the magnetic field source at set increments of one centimeter at a time from 1cm to 5 cm. At each sensor location the wire current was varied from 1 A to 5 A. A plot of sensor voltage as a function of radial distance from wire A is shown in Fig. 4-8. For each location, the applied input voltage to the sensor was kept constant at 8.6 V, and the sensor output signal was recorded.

A theoretical plot of magnetic field versus position and current (Fig. 4-9) was generated using an equation of a magnetic field produced by an infinitely long thin wire (Halliday et al. 2004):

$$B = \frac{\mu I}{2\pi r} \quad (4-1)$$

In Eq. (4-1), B is the magnetic field, μ is the permeability of free space ($1.25 \cdot 10^{-6} \text{ m kg s}^{-2} \text{ A}^{-2}$), I is the current through the wire, and r is the radial position of the sensor measured from the center of the wire.

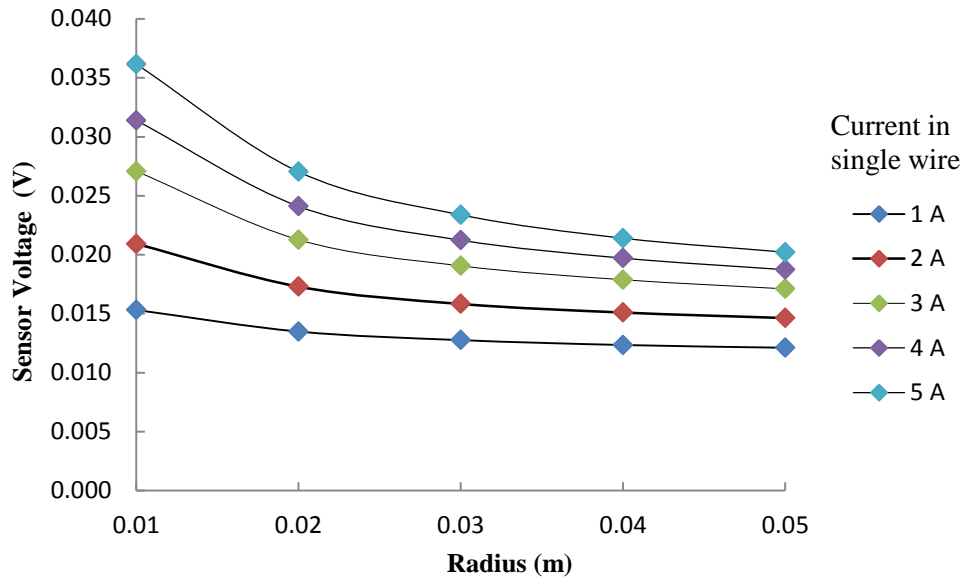


Figure 4-8 AA002-02 sensor voltage vs. position for various currents.

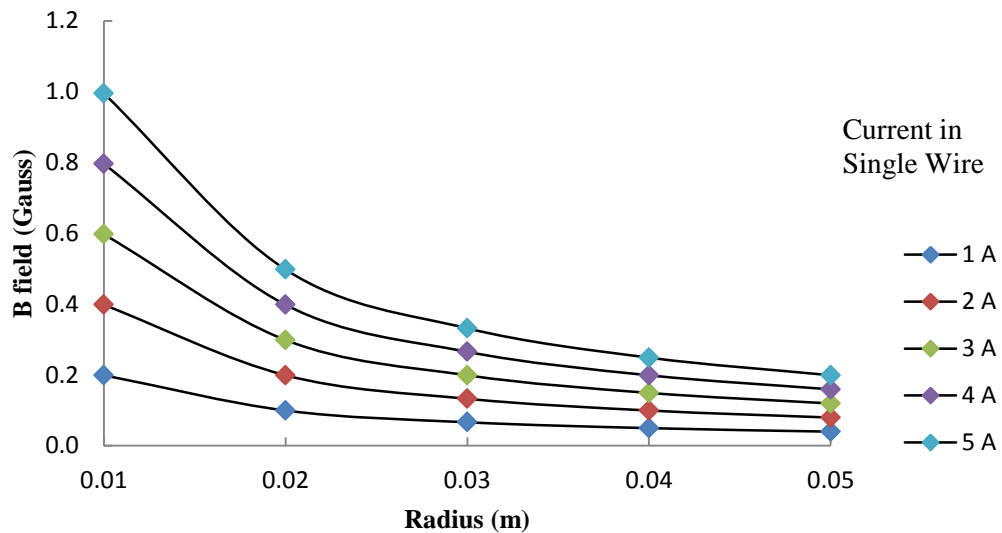


Figure 4-9 Plot of calculated magnetic field at varying sensor positions and current based on Equation 4-1.

Figure 4-8 illustrates that as the sensor is moved further away from the wire, or the wire current is reduced, the change in measured sensor output voltage decreases. This supports the GMR sensor discussion in Section 4.1, which claimed that subjecting a sensor element to a

magnetic field causes element resistance to decrease proportional to the increasing applied magnetic field. When the GMR elements are used in a Wheatstone bridge configuration the measured sensor output voltage decreases with increasing magnetic field. Figure 4-9 shows much higher variation caused by the $1/r$ dependence in Eq. (4-1). The difference between Figs. 4-8 and 4-9 suggests that the sensor output voltage includes an offset, which would be expected in a Wheatstone bridge configuration.

The calibration curve shown in Fig. 4-10 relates the measured sensor voltage change to the applied magnetic field. This plot was constructed from data contained in Figs. 4-8 and 4-9. The linear slope of the plot in Fig. 4-10 can be used to calculate the sensitivity of the sensor as is discussed below. The offset of 0.0132 V explains the visual differences between Figs. 4-8 and 4-9. The magnitude of the voltage change between conditions of no applied magnetic field and applied magnetic field is reported in subsequent plots.

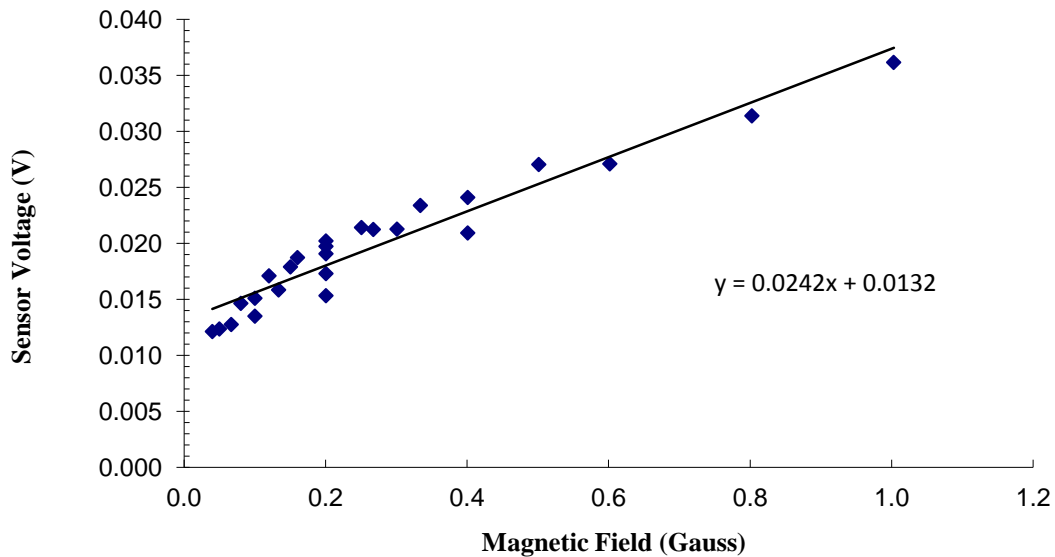


Figure 4-10 Calibration curve for the AA002-02 sensor at an input voltage of 8.6 V.

Based on the AA002-02 sensor information provided by NVE Corporation, when 8.6 V was applied across the sensor, the sensitivity should be approximately 30.9 ± 5.2 mV/Gauss in air. The measured sensitivity shown in Fig. 4-10 of 24.2 mV/Gauss is 21% lower than the one calculated from the NVE literature (NVE, 2012) and just outside the published error band. The measured sensitivity is lower than the expected value because the applied magnetic fields were all lower than the minimum field rating of this sensor of 1.5 Gauss. The y-intercept value of the curve fit equation (13.2 mV) corresponds to an initial sensor offset as mentioned earlier, which is caused by the Wheatstone bridge layout of the GMR sensor elements.

It was discovered that the NVE Corporation sensors were highly sensitive to electrostatic discharge (ESD) and several were destroyed during preliminary testing due to improper handling. Measures were taken to protect the sensors, which included sensor preparation in a static free environment and the use of a Faraday cage during testing to prevent ESD. The Faraday cage was formed by enclosing the sensor breadboard in an aluminum shell that was connected to ground. During discussions with NVE Corporation, they confirmed that ESD is the leading cause of sensor malfunction, and that it is impossible to repair a sensor in the size range used for these experiments after ESD damage has occurred.

4.3 Validation of FEMM Calculations Using Sensors

To replicate results produced by the FEMM tests described in the previous section, the higher range, 10-70 Gauss sensor (AA005-02) was used. To duplicate the higher background magnetic fields produced by an operating Hall thruster, a permanent magnet was placed at a fixed distance from the sensor to provide a constant magnetic field of ~ 70 Gauss. The magnetic field strength at the sensor location was measured using a Gaussmeter. The magnet placement is shown in Fig. 4-11.

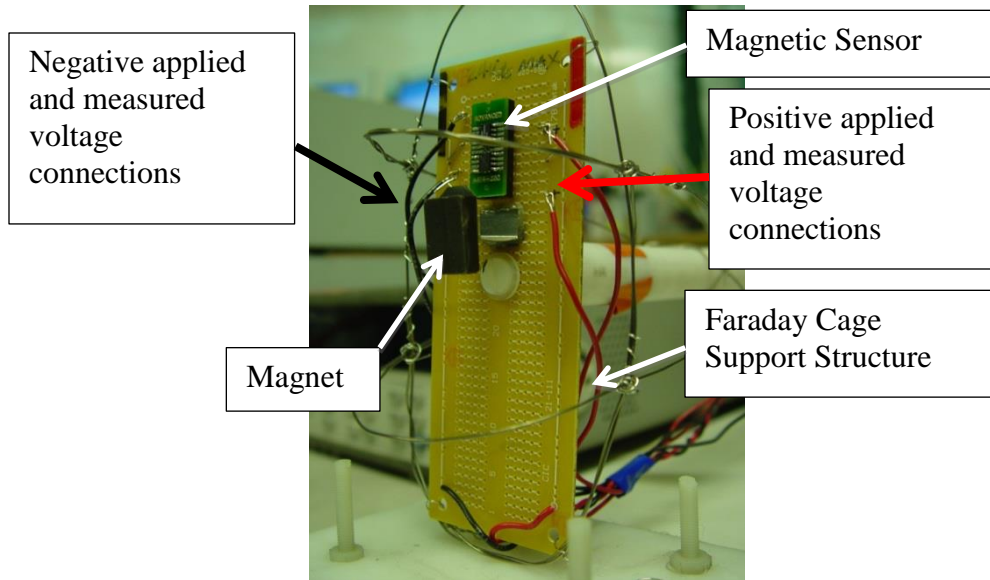


Figure 4-11 Placement of permanent magnet for creating the desired magnetic field for the sensor. Also visible is the framework used to support the foil Faraday cage.

Four tests were conducted using the 10-70 Gauss sensor in the immersed field, including a single wire calibration curve determination test, and three tests to replicate the FEMM simulations reported in Chapter 3. In the calibration curve test, the permanent magnet provided the strong background field (consistent with the field produced at the Hall thruster outer pole piece), while the selected current in the single wire produced small changes in the field (corresponding to the Hall current, which flows during thruster operation). The input voltage to the sensor was increased to 24 volts to maximize sensitivity, which was calculated to be 13.2 ± 2.4 mV/Gauss using NVE Corporation data sheets. Measurements of sensor voltage versus magnetic field strength were created to generate the calibration curve shown in Fig. 4-12. For the test, 11.5 A of current was applied through the single wire while the sensor distance was varied radially from 3.5 cm to 6.5 cm. At each position, a measurement was taken with the current in the wire switched “on” and then “off” to measure the change in voltage registered by the sensor. Since it was hypothesized from the FEMM simulations that a sensor would experience a field

change of about 0.5 Gauss, the wire current was selected to be 11.5 A so as to produce a similar field across the range of sensor position, without overheating the wire. The minimum sensor position of 3.5 cm resulted from the size and shape of the Faraday cage used to protect the sensor from ESD. At each sensor position, several data samples were collected, compared, and averaged for the case where the applied wire current was “off”, and then again when the applied wire current is “on”, to produce the measured change in voltage found at each location. Figure 4-12 shows the collected sensor output voltage plotted against the calculated magnetic field at each location.

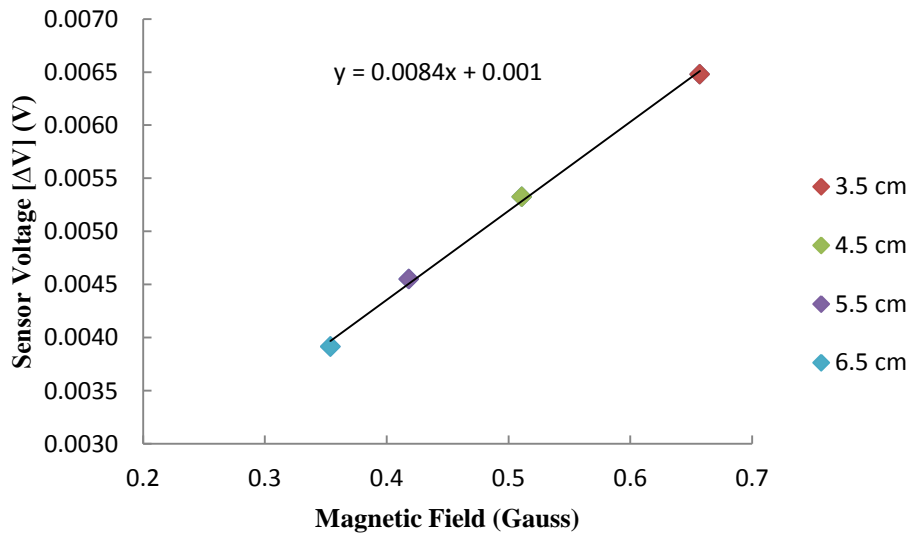
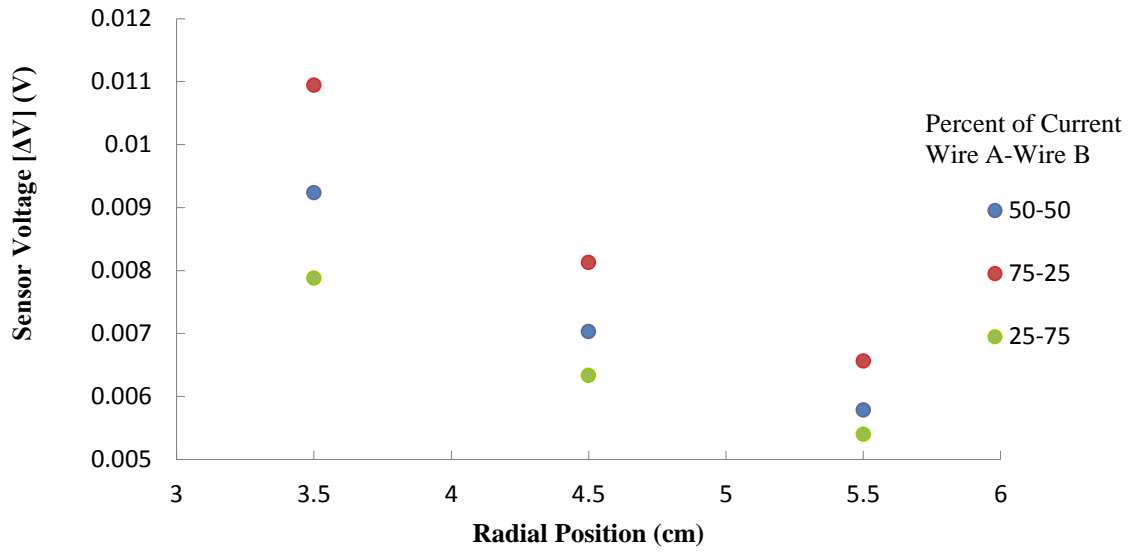


Figure 4-12 Magnetic sensor response to magnetic field induced by 11.5 current flow.

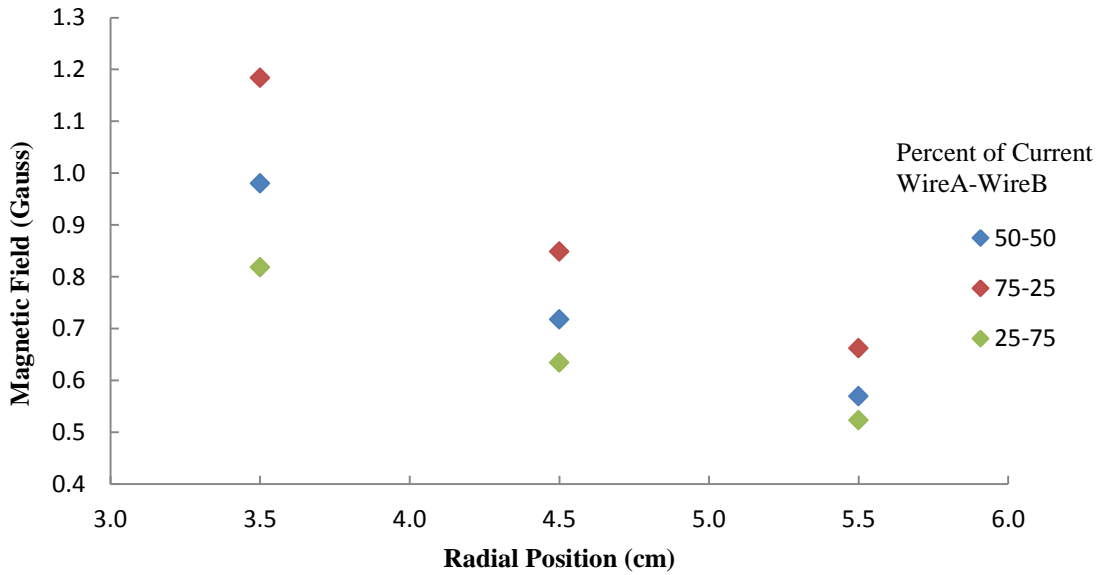
Using the curve fit equation corresponding to Fig. 4-12, the sensitivity is measured to be 8.4 mV/Gauss. This sensitivity is compared to the advertised NVE sensitivity for the AA005-02 GMR sensor, which was given above as 13.2 ± 2.4 mV/ Gauss in air. A 22% error exists between the measured sensitivity and the advertised value, which is outside the advertised uncertainty. It is noted in this regard that the magnet used to create the static background field was not oriented

to be in-line with the axis of sensitivity of the sensor. This likely caused a static field to be outside of the linear region of the sensor sensitivity curve. This issue can be eliminated in the future by employing a better attachment process for the magnet, which consisted of a small piece of magnetic material adhered to the sensor breadboard (visible in Fig. 4-11). All remaining tests will be discussed using the measured sensitivity of 8.4 mV/Gauss.

The next series of tests made use of wire B, placed 2.54 cm further from wire A, mimicking the simulations conducted in Chapter 3. Each wire had 50 % of the total 11.5 A current applied to it, i.e., 5.75 A each. Again, the sensor collected data first with wire current “on” then with wire current “off” for varying radii from wire A over a distance of 3.5 to 6.5 cm. Data were then compared to tests where the total applied current was kept at 11.5 A, but distributed with a higher percentage of applied current to one wire. First 75% of the total current was applied to wire A, with the remaining 25% applied to wire B. Finally, the percent values were switched so that 25% of total current was applied to wire A and 75% was applied to wire B. During both tests, the sensor position was varied and the sensor voltage was measured. To support the FEMM results from Chapter 3, the data were plotted as a function of voltage change versus position for each case of applied wire current. The results of this test are shown in Fig. 4-13. It is observed that the case in which equal current was applied to both wires falls between the cases with un-equal current distributions. Figure 4-14 shows a similar sample collected from the data output of FEMM from Fig. 3-7.



(A)



(B)

Figure 4-13 (A) Sensor voltage versus position for each current assignment. (B) Magnetic field versus position using the calibration curve generated in Fig. 4-12. Total current is 11.5 A for each condition.

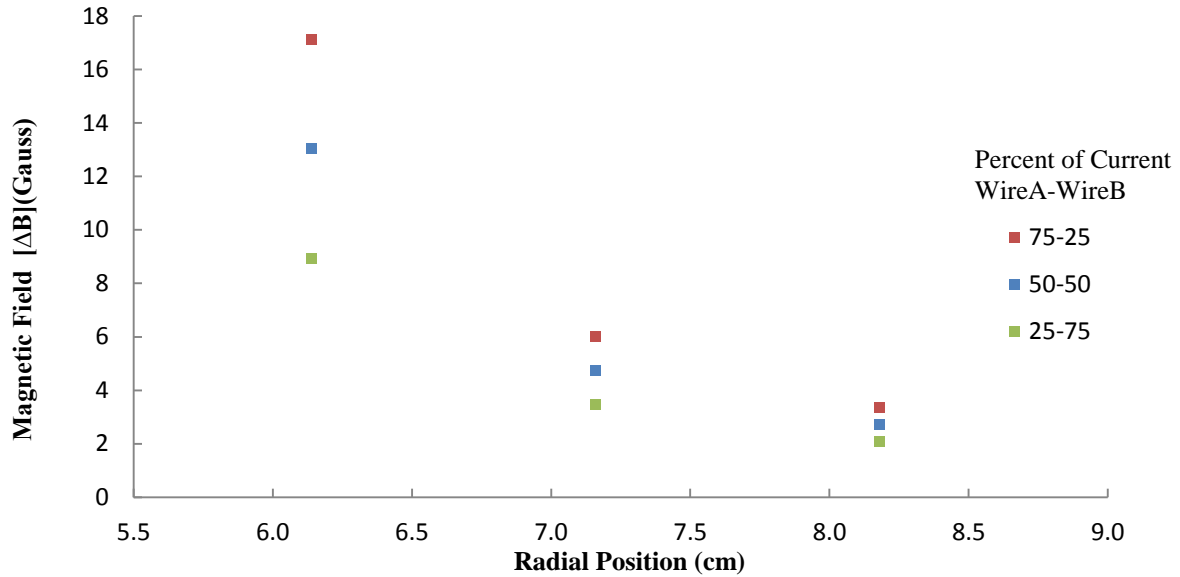


Figure 4-14 FEMM simulation results for three points that are ~1 centimeter apart from the simulated Hall current. These data points were taken from Location (3) in Fig. 3-7.

In each figure, data were collected at a distance of one centimeter apart. It is noticeable in the FEMM results that the measured magnetic field reduces more rapidly than the measured field change from the sensor tests. This is likely caused by the differences between the circular Hall current and the straight wire geometries that are being compared. The data shown in Fig. 4-13 suggest that the NVE GMR sensor is capable of measuring the changes in a static magnetic field resulting from a simulated Hall current.

5. CONCLUSION AND SUGGESTIONS FOR FUTURE WORK

5.1 Conclusion

The calculations and measurements presented in this thesis suggest that the magnetic field produced by the Hall current in a Hall thruster can be measured by magnetic sensors placed remotely in regions above the outer pole piece of a thruster. These results are important because they suggest that remote measurements can be used in an inverse magneto-static algorithm to determine the Hall current density, which in turn can be used to calculate thruster performance. Commercially available giant magnetoresistive (GMR) sensors evaluated with simulated Hall current were shown to be capable of easily measuring changes in a magnetic field of 0.1 Gauss in a background field magnitude of 70 Gauss. A Finite Element Method Magnetics (FEMM) simulation of an SPT 100 Hall thruster was used to calculate that magnetic field changes on the order of 1 Gauss can be induced above the outer pole piece by the presence of the Hall current. This level of change is at least ten times larger than the sensor detection limit. FEMM simulations also suggest that GMR sensors placed above the pole piece will need to function with a background field strength of nearly 50 Gauss. When compared to the test results from various locations in the FEMM simulation, it was concluded that a sensor array could be developed to measure the changing magnetic field of a Hall thruster in operation using GMR sensors. A thrust stand employing a dual hanging pendulum design was also developed in this work. A linear actuator-based, in-vacuum calibration system was used to reduce error caused by thermal drift. The thrust from a low power (1KW) laboratory Hall thruster model running on xenon propellant was measured to within a margin of ± 1 mN.

5.2 Future Work

What the previous four chapters have provided is the information necessary to judge the feasibility of using magnetic sensors to determine Hall current in a Hall thruster. The ultimate goal is to create a non-contact flight hardware device capable of measuring the magnetic field change over a region nearby a Hall thruster in operation. The remainder of this section discusses future work in this area of study.

In maintaining the goal for developing a non-contact magneto-resistive sensor system, future work should be focused on the following categories:

- 1) Inverse Magneto-static Algorithm Development
- 2) Sensor array design and protection

5.2.2 Inverse Magneto-static Problem and Thrust Sensor

The next step in sensor testing would be to replace the long thin wires shown in Figs. 4-5 through 4-7 with current carrying wires placed inside a Hall thruster acceleration channel. Testing would be done by applying balanced and unbalanced current to the wires based on the predicted direction of Hall current with the magnetic coils of the Hall thruster energized. This will provide the sensor with a realistic background magnetic field created by the actual thruster magnetic poles, and a more realistic representation of the Hall current. This work will be relevant to solving the inverse magneto-static problem, which was discussed in Chapter 1, and illustrated in Fig. 1-8 (Rubin et al. 2004). The inversion matrix “A” may be calibrated by moving the wire (or wires) to different axial positions. The calibration results would allow educated guesses to be made of the number of sensors and position of the sensor array that would result in a reasonable

estimation of the Hall current. This sensor array hardware would then be validated using the high sensitivity thrust stand described in Chapter 2. The sensor array development and calibration work would be followed by testing with an actual operating Hall thruster.

5.2.2 Sensor Array Design and Protection

The inverse magneto-static problem requires the collection of measurements over a finite region. Either an array of sensors is required to provide the necessary matrix of magnetic field data, or a single sensor must be fitted on an actuator and moved. The sensor or sensor array will be subjected to several environmental stresses, therefore future work should include measurement of the temperatures and thermal environment at positions along the $R=7.11$ cm and $Z=5.58$ cm contours. This would provide data for designing sensor temperature control such as a possible water cooling system, in addition to whatever required ESD protection is necessary. The sensors used for testing in this thesis are capable of withstanding a maximum operating temperature of $125\text{ }^{\circ}\text{C}$ (NVE 2012). As mentioned before, in addition to adequate thermal protection, careful consideration should be taken in constructing an ESD shield for a sensor array so as to ensure limited interaction with the thruster, and reduce the risk of ESD while the thruster is in operation. Finally, the thruster plume may cause an undesirable interaction with the sensor and ESD shield. Early evaluations should be done to determine if thruster plume and sputtered material would adversely affect sensor performance.

BIBLIOGRAPHY

- Al Sharif, L., Kilani, M., Taifour, S., Al-Qaisi, E., Eleiwi, F. A., Kamal, O. N., et al. (2011). Linear Variable Differential Transformer Design and Verification Using MATLAB and Finite Element Analysis. *University of Jordan, Mechatronics Engineering*.
- Caruso, M. J., Bratland, T., Smith, C.H. , Schneider, R., (1998) A New Perspective on Magnetic Field Sensing. *Honeywell Inc*.
- Choueiri, E. Y. (2001). Fundamental Difference Between the Two Variants of Hall Thrusters: SPT and TAL. *Physics of Plasmas*, 8(11), 5025.
- Dorval, N. (2002). Determination of the Ionization and Acceleration Zones in a Stationary Plasma Thruster by Optical Spectroscopy Study: Experiments and Model. *Journal of Applied Physics*.
- Fruchtman, A., Fisch, N. J., & Raitses, Y. (2001). Control of the Electric-Field Profile in the Hall Thruster. *Physics of Plasmas*, 8(3).
- Garrigues, L., Hagelaar, G. J., Bareilles, J., Boniface, C., & Boeuf, J. P. (2003). Model Study of the Influence of the Magnetic Field Configuration of the Performance and Lifetime of a Hall Thruster. *Physics of Plasmas*, 10(12).
- Gascon, N., Corey, R. L., Capelli, M. A., & Hargus Jr., W. A. (2005). Hall Thruster with an External Acceleration Zone. *International Electric Propulsion Conference*. Princeton.
- Gillard, J. H., Walker, M. L., & Pencil, E. J. (2005). Thrust Stand for Applied Field MPD Thrusters. *International Electric Propulsion Conference*. Princeton.
- Goebel, D. M., Katz, I.,(2008). Fundamentals of Electric Propulsion: Ion and Hall Thrusters. *Jet Propulsion Laboratory*.
- Grubisic, A. N., & Gabriel, S. B. (2010). Development of an Indirect Counter Balanced Pendulum Optical-Lever Thrust Balance for Micro- to Millinewton Thrust Measurement. *Measurement of Science and Technology*, 21(10), 1.
- Haag, T. W. (1997). Thrust Stand for Pulsed Plasma Thrusters. *Rev. Sci. Instrum.*, 68(5).
- Haas, J. M., & Gallimore, A. D. (1999). Characterization of the Internal Plasma Structure of a 5KW Hall Thruster. *University of Michigan, Ann Arbor, Aerospace Engineering. Japan Society for Aeronautical and Space Sciences*.
- Haas, J. M., & Gallimore, A. D. (2002). Considerations on the Role of the Hall Current in a Laboratory-Model Thruster. *IEEE Transactions on Plasma Science*, 30(2).
- Halliday, D., Resnik, R., Walker, J. (2004). Fundamentals of Physics, (7th Edition.) *John Wiley and Sons Inc*.

- Hill, P., & Peterson, C. (1992). *Mechanics and Thermodynamics of Propulsion* (2nd Edition.). Addison Wesley Publishing Company.
- Hirsch, J. E. (1999). Spin Hall Effect. *Physical Review Letters*, 83(9).
- Holman, P. A., (2004) *Magnetoresistance (MR) Transducers and How to Use Them as Sensors Honeywell International Inc*
- Jamison, A. J., Ketsdever, A. D., & Muntz, E. P. (2001). Accurate Measurement of Nano-Newton Thrust for Micropropulsion System Characterization. *International Electric Propulsion Conference*.
- Kato, Y. K., Myers, R. C., Gossard, A. C., & Awschalom, D. D. (2004, December 10). Observation of the Spin Hall Effect in Semiconductors. *ScienceMag*, 306.
- Kleinman, D. A., & Schawlow, A. L. (1960). Corbino Disk. *Journal of Applied Physics*, 31(12).
- Kodys, A. D., Murray, R., Cassady, L., & Choueiri, E. Y. (2006). An Inverted-Pendulum Thrust Stand for High-Power Electric Thrusters. *AIAA*. Sacramento.
- Koizumi, H., Kakami, A., Komurasaki, K., & Arakawa, Y. (2002). A Thrust Stand for Liquid Propellant Pulsed Plasma Thrusters. *Japan Society for Aeronautical and Space Sciences*.
- Longmier, B. W., Reid, B. M., Gallimore, A. D., Chang-Diaz, F. R., Squire, J. P., Glover, T. W., et al. (2009). Validating a Plasma Momentum Flux Sensor to an Inverted Pendulum Thrust Stand. *Journal of Propulsion and Power*, 25(3).
- Meeker, D. (2010). Finite Element Method Magnetics: Documentation. Retrieved 2012, from www.femm.info/wiki/Documentation
- Mikellides, I. G., Katz, I., Hofer, R. R., Goebel, D. M., de Grys, K., & Mathers, A. (2011). Magnetic Shielding of the Channel Walls in a Hall Plasma Accelerator. *Physics of Plasmas*, 18(3), 1.
- Moeller, T., & Polzin, K. A. (2012). Thrust Stand for Vertically Oriented Electric Propulsion Performance Evaluation. *Review of Scientific Instruments*, 81(11), 1.
- Nagao, N., Yokota, S., Komurasaki, K., & Arakawa, Y. (2007). Development of a Two Dimensional Dual Pendulum Thrust Stand for Hall Thruster. *American Institute of Physics*(78).
- NVE Corporation. (2012). Sensor Application Notes. *NVE Corporation: www.nve.com/SensorApps.php*
- Polzin, K. A., Markusic, T. E., Stanojev, B. J., DeHoyos, A., & Spaun, B. (2006). Thrust Stand for Electric Propulsion Performance Evaluation. *Review of Scientific Instruments*, 77(10), 1-7.
- Polzin, K. A., Markusik, T. E., Stanojev, B. J., Dehoyos, A., Raitzes, Y., Smirnov, A., et al. (2005). Performance of a Low Power Cylindrical Hall Thruster. *International Electric Propulsion Conference*. Princeton.

- Popovic, R. S., Drljaca, P.M., Schott, C., (2002) Bridging the Gap Between AMR, GMR and Hall Magnetic Sensors. *23rd International Conference on Microelectronics*, 1, 12-15
- Qarnain, S., & Hastings, D. E. (1997). Complete Computational Model of a Hall Thruster from the Acceleration Channel Through the Plume. *International Electric Propulsion Conference*.
- Raitses, Y., Merino, E., & Fisch, N. J. (2012). Cylindrical Hall Thrusters with Permanent Magnets. *Journal of Applied Physics*(108).
- Raitses, Y., Staack, D., Dorf, L., & Fisch, N. J. (2003). Experimental Study of Acceleration Region in a 2KW Hall Thruster. *39th AIAA/ ASME/ SAE/ ASEE Joint Propulsion Conference*. Huntsville.
- Rocca, S., & Nicolini, D. (2005). Micro-Thrust Balance Testing and Characterization. *International Electric Propulsion Conference*. Princeton.
- Rubin, B. (2006). Analysis and Numerical Experimentation of Onboard Diagnostic Systems for Hall Thrusters. *PhD. Dissertation, Isreal Institute of Technology*.
- Rubin, B., Kapulkin, A., & Guelman, M. (2005). Research on Optimization of Onboard Magnetics Diagnostics System of a Hall Thruster. *International Electric Propulsion Conference*. Princeton.
- Smirnov, A., Raitses, Y., & Fisch, N. J. (2007). Experimental and Theoretical Studies of Cylindrical Hall Thrusters. *Physics of Plasmas*(14).
- Sommerville, J. D., & King, L. B. (2011). Hall-Effect Thruster Cathode Coupling, Part 1: Efficiency Improvements from an Extended Outer Pole. *Journal of Propulsion and Power*, 27(4), 744.
- Thomas, C. A., Gascon, N., & Cappelli, M. A. (2006). Nonintrusive Characterization of the Azimuthal Drift Current in a Coaxial EXB Discharge Plasma. *Physical Review*(74).
- Wetch, J. R., Wong, S., Britt, E. J., McCracken, K. J., & Lin, R. (1995). Improved Hall Type Thruster. *American Institute of Physics*.
- Wilson, M. J., Bushman, S. S., & Burton, R. L. (1997). A Compact Thrust Stand for Pulsed Plasma Thrusters. *International Electric Propulsion Conference*. Princeton.
- Ziemer, J. K. (2001). Performance Measurements Using a Sub-Micronewton Resolution Thrust Stand. *International Electric Propulsion Conference*. Pasadena.